Application of Intensive Light Soaking on Silicon Heterojunction Solar Cells and Modules

presented by

Tobias Rudolph

Master's Thesis in Physics

submitted to the

Faculty of Mathematics, Computer Science and Natural Sciences
Department of Physics of RWTH Aachen University

in June 2022

This thesis was written at the Research Centre Jülich, Institute of Energy and Climate Research, Photovoltaics (IEK-5)

First Examiner
Prof. Dr. rer. nat. T. Hebbeker
Physics Institute III A
RWTH Aachen

Second Examiner
Prof. Dr. rer. nat. U. Rau
IEK-5 Photovoltaik
Forschungszentrum Jülich

Abstract

Silicon heterojunction (SHJ) solar cells are getting increasingly interesting for the industry due to their high efficiencies and easy production steps. To further increase the efficiency of SHJ solar cells, an interesting concept is light soaking at elevated temperatures. It was reported that the open-circuit voltage (V_{OC}) and fill factor (FF) of SHJ solar cells increase during light soaking, which manifests in an efficiency gain. This gain has been observed and explained well by the means of passivation while leaving questions concerning the solar cells' series resistance (R_{S}) reduction. In this thesis, a thermal assisted intensive light soaking process has been proposed as an effective post-treatment method to further enhance the performance of SHJ solar cells. The process parameters influencing the SHJ solar cell is investigated resulting in an efficiency gain of $0.7\%_{\mathrm{abs}}$. A full picture of the passivation and carrier transport properties of SHJ solar cells after light soaking is given. The aim of this work is to give a comprehensive understanding of the mechanism underlying the improvement. The observed enhancements after light soaking are related to increased V_{OC} and FF. The gain of magnitudes is highly dependent on the initial preparation states of the SHJ solar cells. The light soaking impact has been creatively split into thermal and illumination effects. When the temperature during the light soaking process reaches a certain level, the carrier transport loss is reduced, mainly caused by the thermal effect on the enhanced conductivity properties of hydrogenated amorphous silicon (a-Si:H) and transparent conductive oxide (TCO) layers. The improved passivation between the a-Si:H and crystalline silicon interface is induced by carrier injection generated by photos absorption in wafer bulk. It is shown that the light soaking effect remains stable in the solar cells for more than 200 days. This thesis provides an in-depth study of industrial compatible light soaking process and gives insights of how to make good use of it in mass production.

Contents

1 Introduction

The 6th Intergovernmental Panel on Climate Change (IPCC) report published in April 2022 points out how important the reduction of carbon emission is [1]. The goal of limiting the average global warming to 1.5 °C compared to the pre-industrial era that were confessed in the Paris Climate Agreement [2] will not be reached unless appropriate measures are taken [1]. One way to reduce greenhouse gas emissions is to transform the energy sector from fossil fuels to renewable ones. Using photovoltaics (PV) can remarkably lower the emission of greenhouse gasses by 4-5 Gt CO_2 equivalent/year [1]. Due to the enormous developments in production processes, PV systems can pay back the energy invested already after approximately one year of operation [3]. [1] The worldwide cumulative installed capacity for PV at the end of 2021 reached 942 GW with an installation of 175 GW of PV systems in the last year [4]. Roughly 2-10 TW of PV need to be installed by 2030 to keep the rise in global temperature below 1.5 °C [5]. Thus, reliable and high-efficiency concepts are essential to not surpass the 1.5 °C limit and to further increase the impact of PV on reduction of CO_2 emissions.

The highest power conversion efficiency as of date in the class of silicon-based devices is held by the SHJ solar cell. The SHJ concept was developed by Sanyo and presented in 1990 [6]. The cell efficiency showed a steady improvement in the past few years, reaching a value of 26.3% for two sides contacted structure, as reported by Longi [7, 8] and 26.7% for an interdigitated back contact design as reported by Kaneka [9, 10]. Because of its low temperature processes, low temperature coefficient and high bifaciallity, the SHJ solar cell is considered as a promising technology for large-scale terrestrial PV applications [11–13]. Its production contains as few as four main steps: texturing and cleaning the bare wafer, applying the hydrogenated amorphous silicon (a-Si:H) layers by plasma enhanced chemical vapour deposition (PECVD), sputtering the TCO and finally applying the contacts for example by screen printing. The growing commercial interest in SHJ cells has motivated the research in further increasing the power conversion efficiency and understanding the underlying causal mechanisms. High efficiencies are achieved by the outstanding surface passivation and carrier selectivity reached by the use of intrinsic and doped a-Si:H layers, which are the key materials in SHJ solar cells for achieving high voltage (V_{OC}) and fill factor (FF) [14]. In 1977, Staebler and Wronski discovered that light exposure could increase the defect density in a-Si:H, resulting in a performance degradation in thin-film solar

[1] This was observed on commercial available solar cells from European production and operating sites.

cells [15]. This effect raises the concern whether SHJ solar cells manufactured with a-Si:H layers are stable under prolonged light exposure, since the degradation was observed to transfer to the a-Si:H/c-Si interface [16, 17]. In 2016, Kobayashi et al. firstly reported improved performance of finished SHJ solar cells during the first few days of light soaking under 1-sun [18]. The cell efficiency increase was related to improved V_{OC} and FF, which was originated from a reduced density of recombination-active states in the doped a-Si:H/c-Si interface. Recent research shows that through light soaking, the efficiency increases by $0.3 - 0.7\,\%_{\mathrm{abs}}$ [18–22]. Applying a dark forward-voltage bias showed similar kinetics. An increase of the minority carrier injection in the absorber would be generated and may aid in nearby interface-state healing [19, 23].

As demonstrated in recent reports, thermally assisted high-intensity light soaking processes were proposed as a way to accelerate and strengthen the observed enhancement under 1-sun conditions [20, 24]. In industrial production, the processing timescale is on the order of seconds rather than hours, therefore these processes are more suitable. Even though boron-oxigen defects in p-type wafer-based traditional homojunction solar cells resulted in a light-induced degradation, light soaking increased the efficiency of p-type SHJ solar cells efficiently [25]. In addition to publications that emphasize the benefits of the light soaking, there are reports indicating the potential presence of a light-induced degradation mechanism in commercial n-type SHJ solar cells at temperature above 180 °C, or a decrease of the intrinsic/boron-doped (p-type) layer stack hole-selectivity when an insufficiently thick p-type layer is facing the light-incoming side [22, 26].
Despite the beneficial impact on the efficiency of SHJ solar cells, light-induced performance improvement is not yet well understood. Previous studies have focused on defect passivation in the a-Si:H layers to understand the increased V_{OC} and FF. The reduction of active interface defects was attributed to mobile hydrogen ions migrating in the a-Si:H layers under illumination [27]. According to Wolf et al., the presence of a doped layer could motivate the mobile hydrogen ions to migrate toward the interface, while the absence of a doped layer would result in a lifetime decrease due to light-induced defects in intrinsic a-Si:H [16, 17]. Later studies by Bao et al. showed that symmetrical intrinsic a-Si:H passivated c-Si samples retained their lifetime during light soaking, even in the absence of doped layers [20]. Kobayashi et al. reported that UV and blue photons have no influence on the light soaking effect [19]. Cattin et al. showed that light soaking can be detrimental to SHJ solar cells when exposing a p-layer with suboptimal thickness to UV light [22]. Recently, Wright et al. mentioned improved carrier transport in the device after light soaking, and tentatively ascribed it to improved conduction in the contact stack without further confirmation [24]. Boron doped a-Si:H was shown to increase during light soaking [28], and attempts have been made to give an explanation for the observed increases [29]. In order to resolve the previous contradictory reports and reveal the hidden mechanisms of light-induced performance, it is imperative to gain a deeper understanding of the underlying physics of light-induced performance increases.
Most studies focus on either passivation or charge carrier transport. The aim of this

thesis is to investigate the influence of various light soaking conditions on the SHJ solar cells and to identify the sources of the light induced changes. A thermal assisted light soaking at high intensities is adopted and its affect on passivation and carrier transport in SHJ solar cells is investigated. Local carrier extraction properties and material characteristics are analysed in detail to explain the evolution of the current-voltage performance. The observation of the solar cells' behaviour under light soaking has major importance for the usability of the solar cell. The mechanisms behind the improvement need to be understood in order to develop treatments reaching higher efficiencies. To make use of the efficiency gains, the stability of the light soaking effect has to be quantified and its transferability onto modules needs to be investigated.

In this thesis, a fast ($\sim 90\,\mathrm{s}$) and efficient light soaking process is presented to improve the efficiency of solar cells. During the process, a LED based light source with an input intensity of $55\,\mathrm{kW/m^2}$ and two main peaks at 450 nm and 600 nm was used to illuminate the whole area of the SHJ solar cells. The temperature of the sample was elevated to 210 °C by a heating plate. It is observed that both surface passivation and carrier transport can be enhanced after light soaking, the magnitude of the effects depending strongly on the precursors. The light soaking process is decoupled into thermal and illumination effects. It is revealed that the thermal effect is responsible for the R_S reduction, and the passivation improvement is mainly attributed to the illumination effect. Furthermore, it is shown that the light soaking effect will last at least over a period of 200 days on unencapsulated SHJ. Annealing the solar cells at lower temperature (from 125 °C to 175 °C) does not reset the light soaking effect. Choosing higher temperatures (~200 °C) partially resets the effect, suggesting that a part of the light soaking is not reversible and will be maintained through the heat applied in the module encapsulation process.

The outline of the thesis is as follows. Firstly, an introduction of the underlying physics and working principle of SHJ solar cell is given in chapter 2. The most important points and limitations are stated, and the contributions to the total series resistance are discussed. Afterwards, the preparation of the SHJ solar cell as well as the thin-films are described in chapter 3. The characterization and measurement methods such as quasi-steady-state photoconductance (QSSPC), transfer length method (TLM) and conductivity measurement are described in detail. A characterization of the light soaking system is presented in chapter 4, discussing the spectrum used for the light soaking process as well as a temperature calibration. The process parameters are investigated in chapter 5; for this investigation, in house produced solar cells from the IEK-5 baseline are used. The influence of different parameters on the behaviour is investigated in order to obtain the process conditions with the highest gain. Furthermore, the influence of the illuminated side and the sample preparation is investigated. Afterwards, the temperature effect is decoupled from the light induced effect, and the cell performance is analysed systematically in terms of passivation and carrier transport. Additionally, the stability of the light soaking effect is investigated in terms of observing cells stored in the dark. In the last part, the application of light

soaking process to solar cell modules is investigated and discussed in chapter 6. The lamination process and the influence of low intensity light soaking on encapsulated cells is quantified. Lastly, a conclusion and summary of the obtained results is given in chapter 7.

2 Working principle of the SHJ solar cell

In the following chapter, an introduction of the working principle of the SHJ solar cell is presented. The fundamental physical and theoretical aspects are discussed and the main properties of the layers used in the SHJ solar cell are described. The passivation mechanism is revealed and the electrical transport is presented. Further limitations and the resistive properties of a SHJ device are discussed.

2.1 Silicon heteroojunction solar cells

The SHJ solar cell is one of the most common type of passivating contact devices. Record efficiencies of up to 26.3% [7] in a conventional industrial process with both side contacts on full area industrial wafers (246 cm^2) and 26.7% in a back-contact design are reached [10].

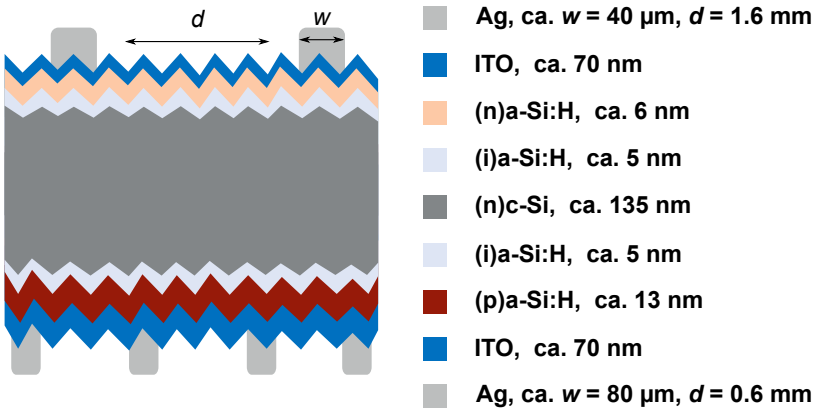

Figure 2.1: Schematic drawing of the band diagram of a SHJ solar cell in IEK-5.

The key to SHJ solar cells' success is the use of a passivating, semiconducting film with a wide bandgap between the highly recombination-active contacts and the crystalline surface [30]. This is archived by depositing nanometre thin layers of undoped hydrogenated amorphous silicon ((i)a-Si:H) on both surfaces by using PECVD. A necessary property for good passivation is that the interface between wafer and a-Si:H film is atomically sharp and epitaxial growth is avoided. The saturation of dangling bonds at the c-Si surface by hydrogen provided by the (i)a-Si:H suppresses surface recombination and yields high V_{OC}. This is known as chemical passivation and improves the

effective lifetime by decreasing the amount of recombination active defects. A-Si:H has a wider band gap than the c-Si, and therefore forming a hetero interface. Theoretically, SHJ devices can reach up to 761 mV [31]. Through the outstanding level of passivation, V_{OC}s above 750 mV [32] have been experimentally reached.
By applying doped layers of a-Si:H and then a TCO on top of the ia-Si:H, the passivation can be increased through the so called field-effect-passivation. In the rear emitter design, phosphorous doped a-Si:H ((n)a-Si:H) is deposited on the top, forming the electron contact and (p)a-Si:H in the rear side forming the hole contact. The boron doped a-Si:H ((p)a-Si:H) forms a depletion region which reaches into the absorber. The band bending in the wafer is further repelling electrons at the hole contact by using (p)a-Si:H and holes at the electron contact by using n doped materials. Through the hetero interface and the doped layers on top of the (i)a-Si:H, selective and passivating contacts are achieved, providing high levels of both field effect and chemical passivation. An approximately 70 nm thick TCO, in most cases Indium Tin Oxide (ITO), is subsequently deposited on top of the a-Si:H layers. The deposition is carried out using physical vapour deposition (PVD). The ITO acts as an anti reflection coating, enables lateral current transport towards the metal electrodes and plays a crucial role in contact formation of the electron and hole selective contacts. The structure of a bifacial rear emitter design fabricated at the IEK-5 is shown in figure 2.1.

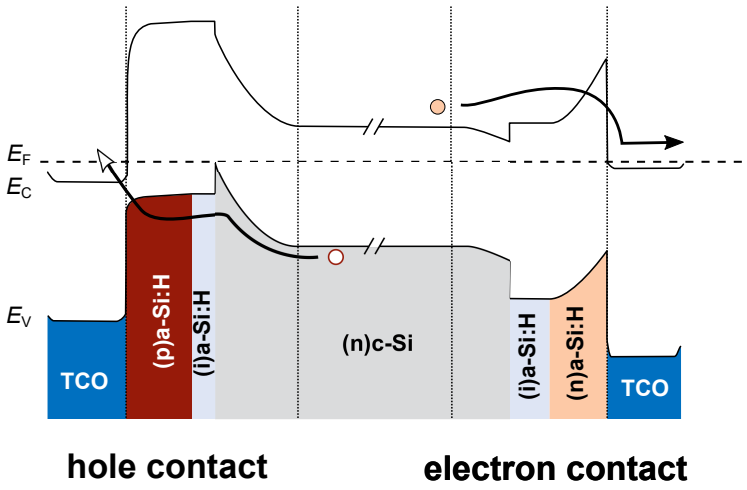

Figure 2.2: Schematic drawing of the band diagram of a SHJ solar cell.

It is important to keep the layers thin, so charge carriers can pass through, but a certain thickness of (i)a-Si:H is needed to guarantee a good chemical passivation. At the same time, the recombination-active metal contacts are shifted away from the bulk, increasing the lifetime [33]. These two considerations enable the high V_{OC} for which SHJ solar cells are known. Too thick layers induce an energetic barrier for charge

carriers and can hamper the current extraction, leading to increased resistive losses within the device and low FF [34]. V_{OC} and FF were reported to decrease rapidly for p-layers as thin as 3 nm, setting a minimum tolerable layer thickness [35]. A too thin a-Si:H(i) layer, on the contrary, leads to insufficient passivation [14]. An optimal thickness (regarding overall solar cell performance) has been found to be about 4 nm [35]. By using a denser and thinner second part of an (i)a-Si:H layer, a reduced vertical rear resistance loss was observed which favours vertical carrier transport and led to a higher FF [36].
The band diagram of a SHJ solar cell is shown in figure 2.2. All available TCOs are n-type, an ohmic contact with n-type a-Si:H can be assured and further increase the electron contact selectivity. This is different for p-type a-Si:H, where the a-Si:H/TCO interface must rather allow for efficient band-to-band tunnelling, where holes collected from the c-Si base into the p-type a-Si:H layer recombine with electrons from the TCO [37]. The doping of the ITO weakens the hole contact by decreasing the field effect passivation. Additionally, the TCO on the rear side acts as a back reflector.

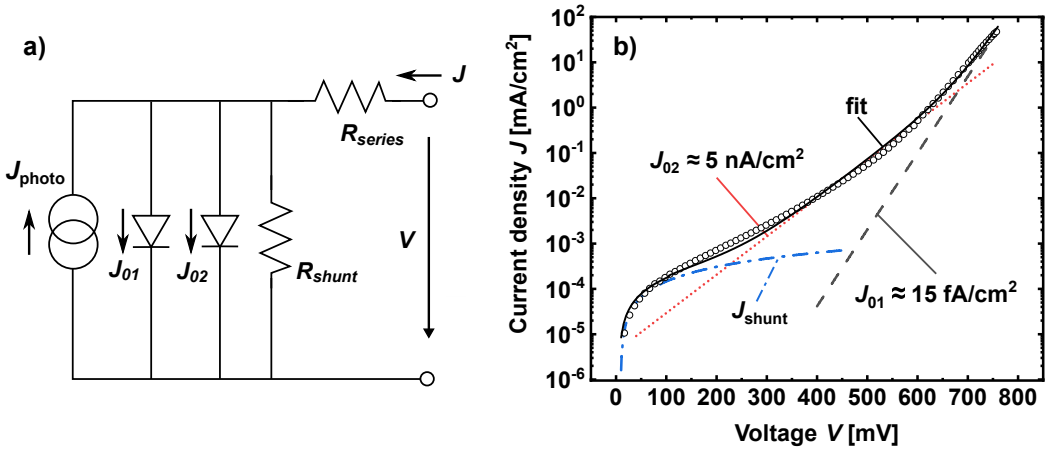

Figure 2.3: a) Schematic drawing of the equivalent circuit of the two-diode model for a solar cell. b) $J(V)$-characteristic of solar cell plotted in logarithmic scale with an exemplary two-diode model fit.

The maindraw back in SHJ solar cells is a lower current density than conventional structures due to parasitic absorption in a-Si:H and ITO layers [14]. The lifetime of minority carriers generated in the a-Si:H layers is very short, particularly in the doped layers, so that absorption in these layers is mostly parasitic. This is less problematic at the rear of the solar cell, since the wafer absorbs almost all light in the visible region. The low-temperature process does not permit the wafer gettering which is performed for homojunction devices fabrication, therefore materials with high bulk lifetime are needed. In addition, low-temperature pastes have higher silver contents, making them more expensive compared to high temperature silver pastes and usually exhibiting lower electric properties [14]. The use of indium is also problematic, as it is a rare material, whose price is unstable [38]. At the module level the interconnec-

tion of SHJ solar cells cannot be done by standard soldering since the temperature is too high, but two alternatives are proposed based on the SmartWire Connection Technology from Meyer Burger or ribbons gluing with conductive adhesive [39].

The light current-voltage ($J(V)$) characteristics of a passivated solar cell can be modelled by a p/n diode in the dark, shifted by a photo generated current density [40]. The equivalent circuit for a solar cell in means of the two-diode model is shown in figure 2.3 a). The two-diodes model has distinct ideality factors n_{id} which account for different recombination mechanisms leads to

$$J(V) = J_{01}\left(\exp\left(\frac{q(V - J(V)R_{\mathrm{S}})}{n_1 kT}\right) - 1\right) + J_{02}\left(\exp\left(\frac{q(V - J(V)R_{\mathrm{S}})}{n_2 kT}\right) - 1\right) + J_{\mathrm{shunt}} - J_{\mathrm{photo}} \tag{2.1}$$

with

$$J_{\mathrm{shunt}} = \left(\frac{V - J(V)R_{\mathrm{S}}}{R_{\mathrm{p}}}\right). \tag{2.2}$$

In the following, it is assumed that ideality factor $n_1 = 1$ and $n_2 = 2$ and the saturation currents J_{01} and J_{02}, which are fitting values obtained from the $J(V)$ in the dark as indicated in figure 2.3 b). J_{01} is interpreted as the diffusion recombination current and J_{02} as the space charge recombination current [41] modelled with two diodes to account for recombination at the wafer surface and in the space charge region respectively. Recombination plays an important role in the performance of solar cells. Passivization is important for V_{OC} and the resistive free pseudo FF (pFF) and therefore the FF. One key of creating an effective heterojunction is a defect free interface, avoiding minority carrier recombination via traps and therefore guaranteeing the maximum quasi quasi-fermi-level splitting in the absorber. A high Schottky barrier between (p)a-Si:H and n-type TCO reduces the probability of hole tunnelling. This is hindering the hole transport and degrades both the V_{OC} and FF [42–44]. In figure 2.4 the band diagram for the TCO/(p)a-Si:H contact is shown. The built-in voltage V_{bi} can be obtained by using the Anderson model and expressed as [33]

$$V_{\mathrm{bi}} = \frac{(\chi_{\mathrm{c\text{–}Si}} - \chi_{\mathrm{a\text{–}Si:H}})}{q} + \frac{kT}{q}\left[\ln\left(\frac{p_{\mathrm{a\text{–}Si:H}}}{N_{\mathrm{V,a\text{-}Si:H}}}\right) - \ln\left(\frac{p_{\mathrm{c\text{–}Si}}}{N_{\mathrm{V,c\text{–}Si}}}\right)\right]. \tag{2.3}$$

Here, the work functions of the c-Si is $\chi_{\mathrm{c\text{–}Si}} \approx 4.05\,\mathrm{eV}$ and of the (p)a-Si:H is $\chi_{\mathrm{a\text{–}Si:H}} \approx 3.9\,\mathrm{eV}$, the Boltzmann constant k, the temperature T, the charge-carrier concentration of the c-Si $p_{\mathrm{c\text{–}Si}}$. The band gap of the (p)a-Si:H is assumed to be, $E_{\mathrm{g,a\text{-}Si:H}} \approx 1.7\,\mathrm{eV}$ and the band gap of the c-Si is $E_{\mathrm{g,c\text{–}Si}} \approx 1.12\,\mathrm{eV}$.

One approach to increase the hole transport is to modify the work function of the TCO. A high work-function TCO is necessary at the rear TCO/(p)a-Si:H interface for high-quality passivation of the hetero-interface [45]. Another approach would be

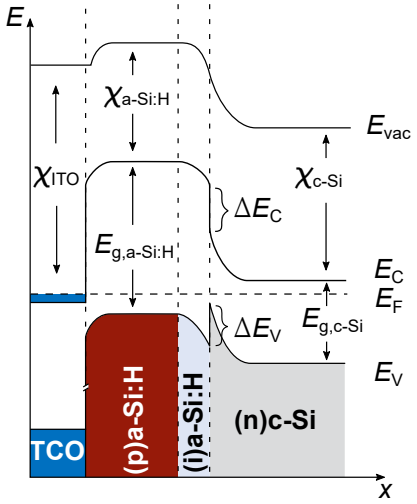

Figure 2.4: Band diagram of the rear side consisting of a TCO/(p)a-Si:H/(i)a-Si:H/(n)c-Si stack is shown.

to increase the doping of the (p)a-Si:H layer, which will lead to a higher build in voltage and better charge extraction due to the higher band bending in the c-Si [44]. Therefore, the hole contact is often the key challenge in building a good device. A well-designed interface between (p)a-Si:H and n-type TCO is the key to a proper working a-Si:H/c-Si device. Regarding the transport of charge carriers across the interface, both (p)a-Si:H and TCO need to feature a high doping concentration, at least at their junction [46]. If the p-layer is sufficiently thick or high doped, the depletion through the TCO can be avoided [47]. For the understanding of the resistive properties, an introduction is in the next chapter.

2.2 Resistivity of SHJ solar cells

The SHJ solar cell structure uses several layers in between the absorber and the metallic electrodes at both sides. The present hetero-interfaces involve complex transport mechanisms in the transverse direction. These mechanisms are not yet fully understood and are generally described as a combination of phenomena such as tunnelling, intra-band tunnelling, band-to-band tunnelling, trap-assisted tunnelling, thermionic emission and hopping [48]. In conventional silicon solar cells, most of the lateral transport towards the metallization grids occurs in the highly doped emitter. SHJ solar cells have very thin and highly resistive emitters but feature TCOs enabling lateral transport. To obtain good contacts, band continuities play an important role and the design of the band offsets are key to lower the series resistance while maintaining high selectivity. The rear emitter design benefits from the lateral transport in the TCO on the front side. Therefore, the TCO on the front side needs to be highly conductive and at the same time highly transparent. The use of a high work function

TCO on the rear TCO/(p)a-Si:H interface enables a high passivated hole contact [49].

To quantify the R_S of the SHJ solar cells, the R_S must be measured. Multiple measurement procedures are available to obtain a R_S. At the IEK-5, the multi-light method is performed as described in chapter 3.3. The SHJ solar cells at the IEK-5 are designed busbar-less. The finger resistance can be neglected thanks to the Grid touch measurement [50].

The lateral transport occurs in the bulk c-Si and the TCO. It is therefore a coupled resistance by the sheet resistance by the ITO and the c-Si bulk sheet resistance and can be expressed as [51]

$$R_{\text{sheet}} = \left(\frac{1}{R_{\text{sheet,TCO}}} + \frac{1}{R_{\text{sheet,c-Si}}} \right)^{-1} . \tag{2.4}$$

The sheet resistance of the c-Si $R_{\text{sheet,c-Si}}$ is known by either the doping level or can be obtained by, for example, QSSPC measurements. The TCO sheet resistance $R_{\text{sheet,TCO}}$ can be either obtained by Hall measurements, by TLM measurements or by 4-point-probe, which will be used in this thesis and is described in the next chapter. The vertical resistance is mainly influenced by the contact resistance ρ_c and can be obtained by TLM measurements. This will be discussed in chapter 3.5 and dedicated samples are prepared as discussed in chapter 3.3.

3 Experimental methods

This chapter describes details of the samples prepared for material characterization, tools used for thin-film deposition and solar cell fabrication, measurements conducted for the material properties and solar cell performance.

3.1 Fabrication process of SHJ solar cells

The fabrication of the SHJ solar cells at the IEK-5 starts from "M2+"-size (157.35 mm x 157.35 mm) n-type Czochralski (CZ) crystalline silicon wafers with a resistivity of 1-5 Ωcm and a thickness of 150 µm purchased from Longi. The wafers were chemically etched to remove saw damage, then textured in alkaline solution to obtain a random pyramid structure on both sides. An ozone cleaning was performed followed by a dip in a 1% diluted hydrofluoric acid solution. For the deposition of the a-Si:H layers, the samples were immediately transported into a PECVD tool (AK1000 from Meyer Burger). Separate chambers for the p-type and n-type layers were used to avoid cross contamination.
On the front side, ~ 4 nm (i)a-Si:H and ~ 4 nm (n)a-Si:H were deposited as passivation and electron contact layer. For the rear side, two types of cells were produced. In "type 1" cells, a H_2-plasma treatment was applied prior to the (i)a-Si:H layer deposition. For the "type 2" cells, this treatment was omitted. In any way, ~ 6 nm (i)a-Si:H and ~ 13 nm (p)a-Si:H layers were deposited as the passivation and hole contact layer on the rear side. This contact is shown in figure 2.4. To avoid a Schottky contact between the a-Si:H the metal contacts and to obtain a high lateral conductivity, a TCO is needed on both sides. A 70 nm ITO layer is sputtered from a 3% Sn-doped In_2O_3 target onto both sides of the solar cell. The sputtering process can damage the passivation, therefore an annealing treatment is important which will be carried out within the screen printing [52]. Silver grids with a busbar less design were screen printed on both sides of the ITO layers. The fingers have a width of 40 – 50 µm and a finger pitch of 1.6 mm on the front side and a width of 80 µm with a finger pitch of 0.6 mm on the rear side. The cells were annealed at 175 °C for 40 min in air atmosphere to cure the silver paste and heal potential obtained sputter damages from the ITO sputtering.

For the investigation of the passivating and conducting properties, several samples geometries are prepared. For the investigation on the passivation properties, (n)c-Si wafers in M2+ size are textured and cleaned. On both sides, (i)a-Si:H layers of approximately 7 nm are deposited by PECVD. For further investigation of the passivation mechanisms, cell structures consisting of a layer structure of (n+i)a-Si:H/c-Si/(i+p)a-

Si:H are prepared as described above, missing out the metallization.

TLM patterns as are prepared on 78 mm × 78 mm test samples for the characterization of charge carrier transport. Eight rectangle pads with a width w = 1 cm and length l = 0.2 cm and a spacing range from 0.5 – 11 cm in steps of 0.1 mm are used. The preparation is analogue to the SHJ solar cell. For the TCO sputtering, a customized mask is used to exclude the area of the contact pads. Afterwards, the Ag contacts are screen printed as in the SHJ solar cells. For the electron contact n-type wafers are used and for the hole contact p-type wafers are used as described in chapter 3.5.

Conductivity measurements are performed on the layers, which are deposited by PECVD on corning glass. The samples undergo a corresponding treatment and the silver contacts are deposited by evaporation. For the characterization by Time-of-flight secondary ion mass spectroscopy (SIMS) as well as electrochemical capacitance-voltage profiling (ECV) layers are deposited on polished float zone wafer in the same PECVD processes as the solar cells.

3.2 Encapsulation of solar cells

To make use of solar cells for electric generation, several cells are connected to strings and these strings in parallel to a module to obtain high currents and voltages. At the IEK-5, light weighted and flexible modules are investigated among others. The encapsulation provides protection for the solar cell from environmental impacts such as water. Soldering of the contacts is a key challenge in passivation based designs since the passivation can be harmed at too high temperatures. Therefore, lamination encapsulation and contacting takes place at temperatures below 250 °C to maintain the solar cells' passivation. Subsequently, the SHJ solar cells are laminated in a sandwich consisting of the SHJ covered with the interconnection layer. Followed by an encapsulation material, Thermoplastic-Poly-Olefin (TPO) covered by a front sheet, and a white back sheet. This stack of front sheet, TPO, connection layer, SHJ solar cell, connection layer, TPO and back sheet (FBS) is laminated at 125 °C for 16 min. The front sheet should be transparent and the back cover can be used as a back reflector.

3.3 Characterization of solar cells and modules

To characterize solar cells for their properties, the LOANA system by pv-tools is used at the IEK-5. It is possible to measure $J(V)$-characteristics as well as the external quantum efficiency (EQE), reflection R and internal quantum efficiency IQE. The main properties will be discussed in the following section.

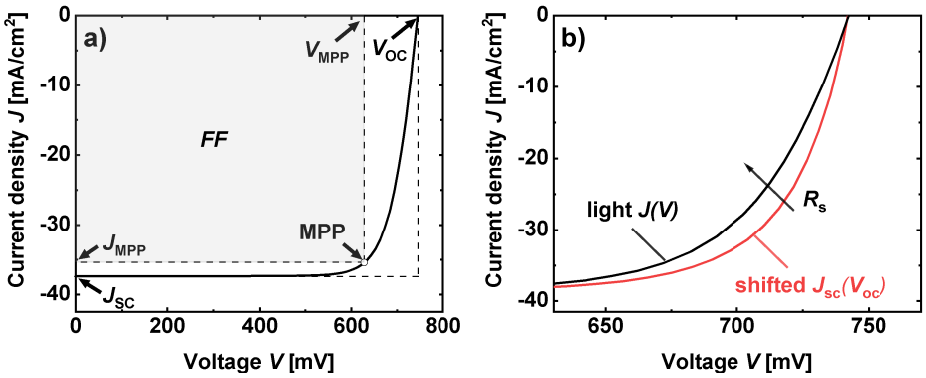

Figure 3.1: In a) the $J(V)$-curve of a typical solar cell and important parameters is shown. In b) the enlarged region of 500-750 mV of a $J(V)$- and a $J_{SC(V_{OC}}$-curve is shown to visualize the influence of the R_S on the $J(V)$ characteristics.

$J(V)$-measurements

To monitor the characteristics of finished solar cells, the $J(V)$-characteristics gives valuable insight into the solar cells' properties. Important figure of merits like η, FF, J_{SC}, V_{OC} and R_S can be measured. Therefore, the M2+ solar cell is placed on a golden reflection chuck and contacted with a grid of 12 busbars and a voltage sense. The illuminated $J(V)$-curve is measured at a stabilized temperature of ~ 25 °C. The most important figure of merit of a solar cell is the power conversion efficiency η. The efficiency is defined as the ratio of obtained power at the maximum power point (MPP) over input power P_{in} as

$$\eta = \frac{J_{MPP} V_{MPP}}{P_{in}} \tag{3.1}$$

The input power is defined by a reference spectrum corresponding the AM 1.5G and is provided by a LED light source by wavelabs Sinus 120 and equals $P_{in} = 1000\,W/m^2$. The V_{MPP} and J_{MPP} are extracted at the points where the power, the deviation of the curve, reaches its maximum as shown in figure 3.1.

Another important characteristic of a solar cell is the fill factor FF which is a measure of squareness of the $J(V)$-curve and is limiting the extraction on maximum power point. It can be expressed as

$$FF = \frac{J_{MPP} V_{MPP}}{J_{SC} V_{OC}} \tag{3.2}$$

with the short circuit current density J_{SC} and the open circuit voltage V_{OC}. With

equation 3.2 the efficiency can be expressed as

$$\eta = \frac{J_{SC} V_{OC} FF}{P_{in}}. \tag{3.3}$$

An example of a $J(V)$-curve is shown in figure 3.1 a). The FF strongly depends on the series resistance R_S and the shunt resistance R_p and is mainly affected by charge carrier transport losses [53], as indicated in figure 3.1 b). To analyse the behaviour of the FF without its resistive losses, the V_{OC} in dependence of the J_{SC} is measured. This will result in a diode behaviour without the influence of the R_S since the curve is measured in V_{OC} conditions. The obtained FF of this so-called $J_{SC}(V_{OC})$-curve is referred to as the pseudo fill factor pFF. The difference of the $J(V)$- and the $J_{SC}(V_{OC})$-curve is shown in figure 3.1 b). To obtain the R_S several methods can be used. One method is to subtract the pFF from the FF which gives reasonable results at MPP as [53]

$$R_S(V_{MPP}) = (pFF - FF)\,\frac{J_{SC} V_{OC}}{J_{MPP}^2}. \tag{3.4}$$

However, assuming that the R_S as a constant value over the whole $J(V)$-curve is an oversimplification, therefore methods as the so-called multi-light-method [54] will be used in the thesis. To obtain the R_S, n numbers of $J(V)$-measurements are executed at multiple light intensities with slight higher and lower intensities as 1-sun. The R_S is evaluated over the whole measurement range and obtained by [54]

$$R_S(J) = \left| \frac{\sum_{i=1}^{n} (V_i - \overline{V})^2}{\sum_{i=1}^{n} (V_i - \overline{V})(J_i - \overline{J})} \right| \tag{3.5}$$

where V_i and J_i are the voltage and current of each involved $J(V)$ curve, $\overline{V}$ and $\overline{J}$ are the average voltage and current density, all for given light intensities. This method provides higher accuracy because the measurement is performed at similar illumination intensity to actual operating conditions, and thus the error from variation due to dependence on injection levels is minimized [54]. It should be noted that the multi-light-method measures the differential R_S and not the absolute value. The difference between actual and differential R_S can be regarded as rather small [55].
Concerning the measurement of modules, the actual module temperature during the $J(V)$-measurement may not be accurately reflected since the PT1000 temperature sensor does not directly contact the solar module. This may cause a small deviation of V_{OC} which is assumed to be ignoble small [56].

Quantum efficiency measurement

The external quantum efficiency EQE gives insight into the collected charge carrier per incident photon. It can be measured by measuring the J_{SC} at every wavelength. This can be done by using an artificial light source (tungsten- and wolfram-lamps) and a monochromator. Together with the reflectance R the internal quantum efficiency

can be calculated via

$$IQE(\lambda) = \frac{EQE(\lambda)}{1 - R(\lambda)} \tag{3.6}$$

which is a measure for the collected charge per collected photon.

3.4 Quasi-Steady-Sate Photo Conductance

The time photogenerated charge carrier exist in the c-Si bulk before recombination is referred to as effective lifetime τ_{eff} and is given by the overall lifetime in the c-Si bulk τ_{bulk} and at its lifetime influences of its surfaces by

$$\frac{1}{\tau_{\text{eff}}} = \frac{1}{\tau_{\text{bulk}}} + \frac{2D}{S_{\text{eff}}}. \tag{3.7}$$

with the thickness D and the surface recombination velocity S_{eff}. The bulk lifetime is reesembled by different recombination processes as the radiative recombination, Schokley-Read-Hall recombination by traps in the energy band and Auger recombination. A WCT-120 from Sinton Consulting [57] is used to perform QSSPC measurements. QSSPC is a fast and reliable method to measure the effective lifetime τ_{eff} of minority charge carriers in a semiconductor [57]. A light pulse is increasing the photo-conductivity homogeneously over the sample. The generation of charge carriers is monitored by a coil which is conductive coupled to the sample through an oscillating circuit.

A measure for passivation is the implied circuit voltage, iV_{OC} which is a limit for the devices V_{OC}. It resembles the quasi-fermi-level splitting in the semiconductor which is influenced by the recombination and excess charge carrier generation and can be expressed as

$$\text{i}V_{\text{OC}} = \frac{k_{\text{B}}T}{\text{q}} \ln\left(\frac{(\Delta n + N_{\text{A}})\Delta n}{n_{\text{i}}^2}\right) \tag{3.8}$$

where k_{B} is the Boltzmann factor, T the temperature, q the electron charge, Δnmthe generated excess charge carriers and N_{A} and n_{i} is the intrinsic carrier density.

From the $\tau_{\text{eff}}(n)$ information about the passivation mechanism can be concluded. While the density of interface states leads to a global up- or downward shift of the effective lifetime curve, the impact of the field effect is injection dependent [23]. For high injection levels, the bands are flattened as the mobile excess charge carriers are relocated and thus effectively shield the fixed charges, which reduces the passivating field effect. Thus, a band bending will predominantly impact the low n range and leads to a tilting of the $\tau_{\text{eff}}(n)$ curve [58].

3.5 Electrical characterization

In the following chapter, the electrical characterization methods for thin films and half processed devices are described. The conductivity measurement of thin doped a-Si:H films is explained, the procedure of the TLM measurement is discussed as well as the sheet resistance measurement. Finally, the ECV measurement procedure is explained.

Conductivity

A major property of interest is the conductivity of thin layers. Conductivity measurements give insight about the ability to conduct current and is therefore a measure of the doping and defects in the material. To characterize the (n)- and (p)a-Si:H, lateral conductivity properties samples are prepared on corning glass (CG). The conductivity of CG can be neglected compared to the of doped a-Si:H, which is in the order of 10^{-5} to 10^{-3} S/cm. Co-planar Ag electrodes with a thickness of 700 nm were evaporated on the layer. For a valid measurement, the contact needs to show an ohmic behaviour. The conductivity is measured by applying a voltage V on the electrodes and measure the lateral current J. The conductivity can then be derived by

$$\sigma = \frac{J}{V}\frac{L}{Wd} \tag{3.9}$$

with and applied voltage of 100 V. The length of the contact pads L, the width W and the thickness of the layer d. In this geometry, $L = 0.5$ cm and $W = 5$ cm and the thickness was measured on several points using an ellipsometer as described in 3.6. If not other stated, all measurements were made in vacuum at a temperature of 293 K, with stabilized conditions. This setup is chosen since the contact resistance is negligible due to the large contact area between the contact pads and the a-Si:H $(l \times w)$ if compared to the cross-section $(d \times w)$ that the current is though the layer.

Transfer Length Method

The TLM is used to derive the specific contact resistivity ρ_c between two different semiconductors [50]. The electron and hole contacts have usually a major contribution to the resulting R_S of the SHJ solar cell [50] and play a cruical role in the design of the SHJ solar cell layers. The used structure to measure the ρ_c consists of multiple layers, as shown in figure 3.2 a). The ρ_c is determined by measuring the $J(V)$-curve over each of the in-equidistant contact pads and then extrapolating a linear behaviour as shown in figure 3.2 b). The total measured resistance is obtained as

$$R_{tot}(d) = \frac{R_{sh}}{w}d + 2R_c \tag{3.10}$$

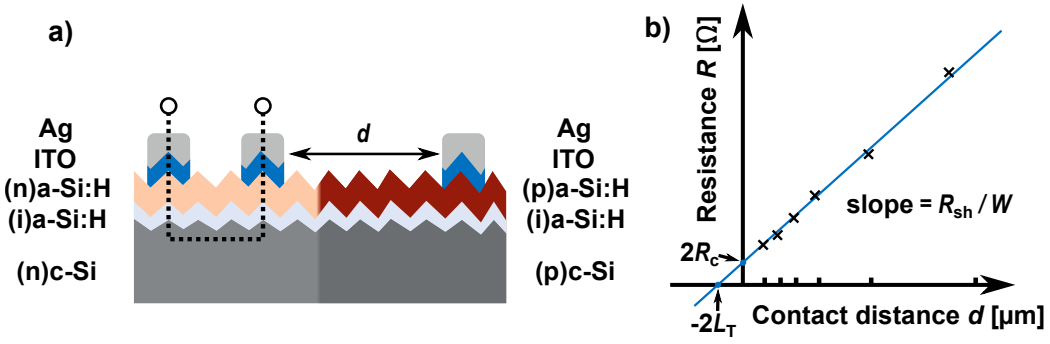

Figure 3.2: a) Sketch of TLM structure for the ρ n-type and the ρ p-type. b) exemplary measurement of the TLM. Plotted is the total resistance against the distance of the contact pads.

with the sheet resistance R_{sh} of the layer stack between the contacts and the contact resistance R_{c}. The ordinate equals $2R_{\mathrm{c}}$ which is a composition of the layers stack contact resistance and resembles the contact at $d = 0$. The so-called contact length L_{T} is then defined through

$$L_{\mathrm{T}} = \sqrt{\frac{\rho_{\mathrm{c}}}{R_{\mathrm{sh}}}} \tag{3.11}$$

which represents the average distance a charge carrier travels in a semiconductor before entering a metal contact. The contact resistance extracted from the ordinate as the resistance value for a zero gap width and can be derived by [59]

$$R_{\mathrm{c}} = R_{\mathrm{sh}} \frac{L_{\mathrm{T}}}{W} \coth\left(\frac{L}{L_{\mathrm{T}}}\right) \tag{3.12}$$

where R_{Sh} is derived of the slope from the $R(d)$ curves. In the case of large contact resistivity compared to the bulk R_{sh} a homogenous current distribution over the contact area $A_{\mathrm{c}} = w \times l$ is forced and $L_{\mathrm{T}} \approx L$. In this case the hyperbolic cotangent function can be assumed to equal unity and therefore the contact resistance is defined by

$$\rho_{\mathrm{c}} = R_{\mathrm{c}} L_{\mathrm{T}} W. \tag{3.13}$$

As indicated in figure 3.2 b), the abscissa intercept is equal $-2L_{\mathrm{T}}$. This procedure is valid only if the pads l are much larger than the transfer length L_{T} to avoid current crowding effects. It has to be verified, that the measured contacts are ohmic and therefore follow a linear $J(V)$ dependence in the measurement range.
It should be noted, that the measured R_{c} can be split into contributions of the metal contacts, the interfaces and the bulk as follows

$$\begin{aligned} R_{\mathrm{c}} = 2\,(&R_{(\mathrm{i})\mathrm{a\text{-}Si:H}} + R_{(\mathrm{p})\mathrm{a\text{-}Si:H}} + R_{(\mathrm{p})\mathrm{a_Si:H/TCO}} \\ &+ R_{\mathrm{TCO}} + R_{\mathrm{TCO/Ag}} + R_{\mathrm{Ag}}). \end{aligned} \tag{3.14}$$

The vertical contribution of the Ag and the TCO to the R_{c} are comparably small and

can be neglected as well as the Ag/TCO contact [50].

To obtain the contact resistivity of electron contact, samples are prepared on an n-type wafer. Since the (p)a-Si:H forms a diode on an n-type wafer, a p-type wafer needs to be used for the measurement of the hole contact [50]. This approach can be assumed as valid since at the (n)c-Si/(i)a-Si:H/(p)a-Si:H contact an inversion layer is existent. The c-Si wafer is in fact p-doped at the surface, thus using (p)c-Si wafers may not represent a strong bias. To simulate the inversion, the doping of the p-type wafer should be high enough.
The assumption is made that the front (n)a-Si:H/TCO contact is not significantly affected by the illumination of the solar cell at V_{MPP} condition, as the metallized finger will shade the contact underneath. Therefore, the front contact is almost the same in dark condition than the TLM measurement.

Sheet-resistance measurement

To obtain insights of a thin layers' sheet resistance, 4-point measurements can be executed. The four co-linear and equidistant contacts are pressed on a thin layer, the outer two contacts apply a current I and two inner measure the resulting voltage V drop. The sheet resistance can be obtained by using [60]

$$R_{\mathrm{sheet}} = \frac{\pi}{\ln(2)} \frac{V}{I}. \tag{3.15}$$

The measured TCO samples are deposited on 10 mm×10 mm corning glass since the sample needs to be about 40 times larger than the probe spacing [60].

Electrochemical Capacitance-Voltage Profiling

The ECV is a technique to measure the active doping concentration of a semiconductor. A Schottky contact is formed between the semiconductor material and an electrolyte, which results in a depletion region. This region is empty of conducting electrons and holes, but contains ionized donors and electrically active defects or traps. Charge is stored and can be measured as in a capacitor. The capacitance as function of voltage it can be calculated with

$$\frac{1}{C^2} = \frac{2(\phi - V)}{\mathrm{q}\epsilon_0\epsilon_{\mathrm{r}} A^2 N_{\mathrm{D}}} \tag{3.16}$$

where ϕ is the contact potential, V is the voltage and N_{D} active doping concentration. Which can be transformed into

$$N_{\mathrm{D}} = \frac{1}{\mathrm{q}\epsilon_0\epsilon_{\mathrm{r}} A^2} \frac{C^3}{dC/dV} \tag{3.17}$$

with the vacuum permittivity ϵ_0 and the relative permittivity ϵ_r and the area of the contact A. The accuracy of the measurement depends on the accuracy of the contact area, which is defined by a $1\,cm^2$ plastic sealing ring [61]. To obtain a depth profile, the semiconductor is electrolytically etched between the capacitance measurements. As the etching solution, a 0.1 molar ammonium hydrogen fluoride (NH_4HF_2) was used. For the (n)a-Si:H etching, light is used and for (p)a-Si:H voltage etching is used. The (p)a-Si:H material must be carefully etched with sufficient large etching currents to avoid rough, porous or unequal etching. The (p)a-Si:H tends to etch at the sealing ring, which can be avoided by dipping the sample into 1% hydrofluoric acid (HF) until the surface is H_2 terminated. A hydrophobic surface is obtained and therefore leaking at the sealing ring is avoided. The etching depth is determined according to the amount of the removed substance, obtained from Faraday law

$$d = \frac{M}{zF\rho A} \int_{t=0}^{t=t_{max}} I(t)dt \tag{3.18}$$

with the molar mass M, the valence number of substance ions z (the amount of electrons, which is needed for one molecule to dissolve), the Faraday constant F, the material specific density ρ, and the surface A. The etching current was at the level of $0.5\,mA/cm^2$ at $3\,V$ and therefore above the porous etching peak of Si.

3.6 Thin film characterization methods

Secondary Ion Mass Spectroscopy

SIMS is a valuable technique to measure atom concentration in films. A primary ion beam of Cs+ is used to sputter secondary ions from the target material. The secondary ions are accelerated in an electric field. Due to the sputtering, it is possible to perform depth measurement of atom concentrations in thin films. Quantification of the atom concentration is possible if a standard sample of the investigated material with a known atom concentration can be measured. SIMS shows the concentration of all dopant atoms in the sample, which can be compared with ECV measurements which show the activated dopants. SIMS is used to measure hydrogen and boron concentrations in the a-Si:H layers. For the measurement of the boron concentration, an unintentionally doped thick layer with a known dose of ion implanted boron is used for quantification. The measurements are performed at the central institute for engineering and analysis 3 of the research centre Jülich with an ToF-SIMS IV by IONTOF.

Ellipsometry

Ellipsometry is a fast and easy method to measure the thickness of a thin film. Parallel and perpendicular polarized light is used to obtain the phase difference Δ and the amplitude diminution Ψ at different angles. With an appropriate model, for example

applying the Tauc-Lorentz theory, the thickness can be derived [62]. Besides the thickness, further parameter can be obtained. For example, one can get information about the band gap (E_g) of the deposited thin film, and the refractive index and the extinction coefficient. A M-2000 Spectroscopic Ellipsometer from J.A. Woollam is used in this work for film thickness determination together with included optical models and data for the material.

Hydrogen effusion

Effusion measurements can give insight to the hydrogen structure and behaviour inside a sample. For effusion measurements, samples are heated by a furnace in a quartz tube with a constant heating of 20 K/min from room temperature to above 800 °C. A turbo molecular pump continuously evacuates the quartz tube. The time derivative of the hydrogen partial pressure is proportional to the hydrogen effusion rate $dN_H/dt = 0.15$. The hydrogen partial pressure is measured by a quadrupole mass spectrometer and a gas friction pressure gauge [63, 64].

3.7 Set-up of the light-soaking oven

The light-soaking oven (LiSO) used in IEK-5 is produced by GSolar. The LiSO is an outline treatment where the cells are inserted in batches. The cells are placed by an automatic absorption on a rail system, which transfers the samples into the preheated chamber. The solar cells are sucked onto the heating table by a vacuum suction to ensure good thermal contact. The process temperature $T_{process}$ resulting in the chamber can be set and regulated over the illumination and the heating table (35 cm×35 cm×5 cm) and by air circulation. The temperature of the table is measured

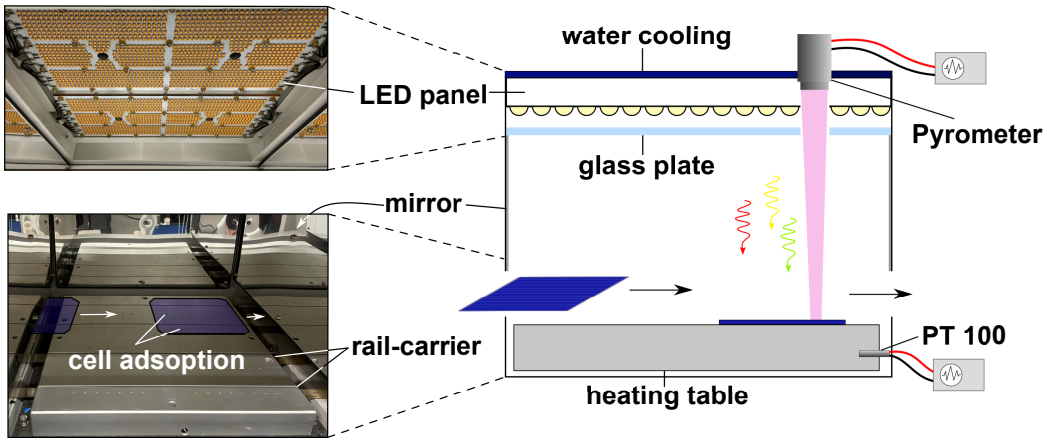

Figure 3.3: Pictures of the LED panel (left upper) and heating table (left lower) and sketch of the LiSO (right).

via an PT 100 in the centre of the table and referred to as T_{table}. The temperature

of the solar cell is monitored by a pyrometer to ensure the process temperature is stable. The illumination source is an LED panel as shown in figure 3.3. To prevent the LED from degradation by the evolved heat during operation, water cooling maintains temperatures below 30 °C.
A glass plate further protects the LED from heat. To avoid scattering losses at the chamber walls, mirrors are mounted onto the insides of the chamber.
For all processes, the LiSO is heated up sufficiently long to obtain a constant illumination spectrum and to avoid temperature fluctuations. The spectrum is in the region of visible light between 400 nm and 600 nm and will be discussed in chapter 4.
In conventional heating, the time-temp profile can be varied to have the optimum temperature profile and does not exceed the thermal budget, which could harm the passivation. The solar cells are inserted in the preheated oven with a lower intensity light, the intensity is then switched on to full power and after the setted treatment time, the solar cells are removed by the automatic grip system. This results in a sharp temperature profile and no overshoots at the heating maximum, as sometimes observed in rapid-thermal annealing processes. A measurement of the temperature profile during the light soaking is discussed in chapter 4. It should be noted that all treatments of solar cells are performed under open circuit conditions.

4 Light soaking system

In the following chapter, the illumination source and the temperature behaviour of the LiSO will be characterized. Therefore, the spectrum is measured, and the pyrometer measuring the process temperature is calibrated using a K-type thermocouple glued on a solar cell. Later, the temperature of an exemplary light soaking process is measured and an equivalent temperature process is described.

4.1 Spectrum characterization

The spectrum in the LiSO is measured via a spectrometer instrument system CAS140CT for various input powers in the range of $1 - 55\,\mathrm{kW/m^2}$. The normalized spectrum is shown in figure 4.1 a) together with the AM 1.5G solar spectrum and the EQE of a SHJ solar cell from the IEK-5 baseline. In figure 4.1 b) the absolute spectral irradiance of the spectrum at input intensities of $1\,\mathrm{kW/m^2}$, $20\,\mathrm{kW/m^2}$, and $55\,\mathrm{kW/m^2}$ is shown. The maximum of the main peak of the spectrum lies at a wavelength of

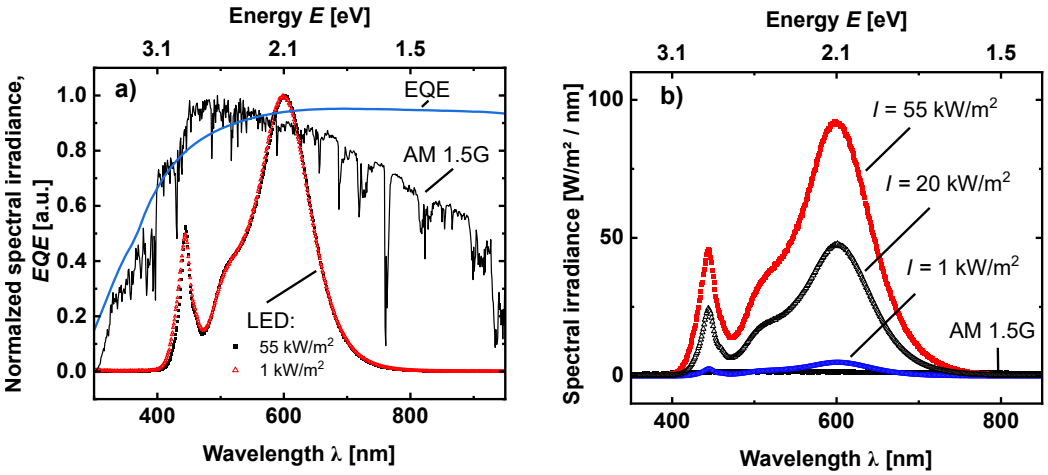

Figure 4.1: a) Normalized spectrum for two different illumination intensities, together with the AM 1.5G sun spectrum and the EQE of a typical SHJ solar cell. b) Absolute spectral irradiance measurement of different light intensities.

600 nm, and the spectrum exhibits another clear observable peak with a maximum at about 450 nm. Its shape is maintained for $1\,\mathrm{kW/m^2}$ and $55\,\mathrm{kW/m^2}$ where it shows slight variation in the range of short wavelengths.
For the spectrum at hand, the number of photons per second and per surface unit is approximately $2.72 \cdot 10^{20}\,\mathrm{m^{-2}s^{-1}}$ at 600 nm.

The absorption coefficient α of c-Si and a typical (n)a-Si:H thin film and the corresponding absorption length L_α, which is the inverse of α, is shown in figure A.1. At L_α, the incident intensity is reduced to $1/e$ of the initial intensity. For photons with a wavelength of 600 nm $L_\alpha \approx 2.42\,\mu m$ in c-Si and $L_\alpha \approx 0.260\,\mu m$ for the a-Si:H layer. The L_α of the a-Si:H layers is much lower than the c-Si; but with a given thickness of 9 nm, only a small fraction will be absorbed by the a-Si:H layers, which is nonetheless significant. Therefore, most of the light can penetrate through the front a-Si:H layers (no matter for n-side or p-side) into the c-Si bulk and will be absorbed in the first 10 µm of the material.
There should be almost no light penetrating through the wafer bulk to reach the a-Si:H layers on the back side of the solar cell. To quantify how much light is penetrating the absorber, a wafer was placed carefully on top of the entrance of the spectrometer. The measured intensity is in the order of $10\,\mu W/m^2$ as shown in figure A.2.

4.2 Calibration and temperature measurement

To ensure that the temperature of the solar cells and samples during the light soaking is well-defined, the heating table temperature is tracked by a PT100. Additionally, a pyrometer is installed to monitor the process temperature of the solar cells. Since the

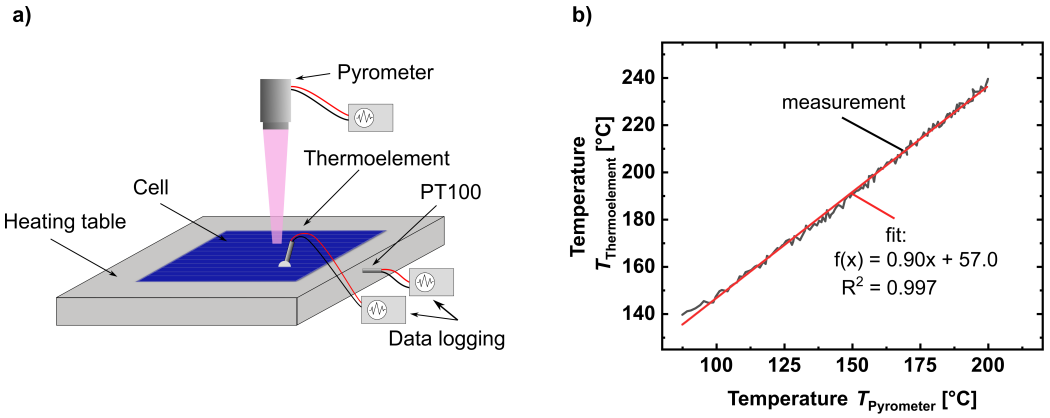

Figure 4.2: In a) a schematic drawing of the temperature calibration is shown. The TE is glued with conductive paste onto the interior of the solar cell, which is sucked to the surface of the heating table. The temperature was varied from RT to a heating table temperature of ~ 250 °C. In b) the measured pyrometer temperature is plotted against the measured TE temperature. The data is described by a linear behaviour.

measured pyrometer signal depends on the observed surface properties, the pyrometer needs to be calibrated to obtain an estimate of the real temperature of the treated solar cells. The set-up is show in figure 4.2 a). A K-type thermoelement (TE), Ni+Cr(10%) for positive polarity and Ni for negative polarity, with a wire thickness of 0.1 mm, is glued on the solar cells' surface with silver conductance paste. The

temperature is logged by using a HOBO single-channel data logger UX100-014M. In order to obtain a valid measurement, the TE must be mounted into the interior of the silicon, and therefore, it is very cumbersome and inconvenient for routine monitoring. It must be noted that the TE needs to be small so that the temperature is determined by the wafer and not by the heat capacity of the TE. Therefore, a wire thickness of 0.1 mm is used. The solar cell is placed on the heating table, and the heat-up from room temperature to 250 °C is monitored using both the heating table and the light source. In figure 4.2 b) the temperature measured from the TE T_{TE} is plotted against the pyrometer signal $T_{\mathrm{Pyrometer}}$. The measured temperature can be fitted by a linear function to obtain a correction function for the pyrometer, as shown in figure 4.2 b). The pyrometer was already set up and calibrated by the manufacturer, which explains the linear behaviour. For the rest of this thesis, the corrected pyrometer temperature by the TE will be regarded as the real temperature. Therefore, the real temperature is obtained by

$$T_{\mathrm{Real}} = 0.90 \cdot T_{\mathrm{Pyrometer}} + 57.0 \tag{4.1}$$

using the measured pyrometer temperature. In the rest of the thesis, the process temperature will be referred to as the recalculated pyrometer temperature.

It is ensured for all processes that the temperature is controlled during the light

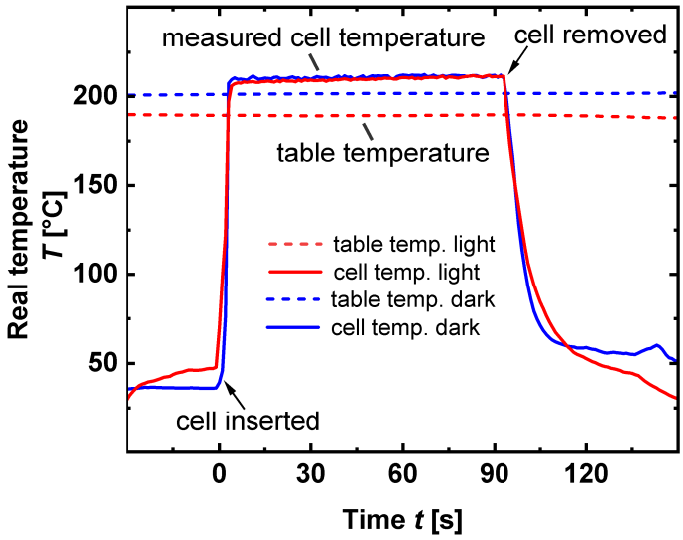

Figure 4.3: Temperature measurement of a 90 s light soaking process (red line) and an equivalent dark annealing process (blue line), both for a resulting process temperature of 210 °C. The dotted lines are representing the corresponding table temperatures.

soaking by using a reference solar cell at the position of the pyrometer. For different surfaces, the temperature calibration will not be valid. The difference of the temper-

ature between polished and an etched surface, for example, is ~ 10 °C. In figure 4.3, a 90 sec light soaking process with 55 kW/m² and a 90 s dark annealing process is shown. As described in section 3.7, the solar cells are placed on a rail-carrier system and are transported through a track onto the pre-heated heating table and are sucked to the table for good thermal contact. For the shown process, the heating table has a set point temperature of 190 °C (the red dash line). The illumination causes the temperature to rise in approximately 4 s from its starting temperature of 47 °C, which is the ambient temperature of the solar cells resting on the tracks in the loading chamber, to the process temperature of 210 °C, which results in a heat up rate of 40.75 °C/s. Thanks to the good thermal conductivity of silicon, the temperature of the solar cells increases sharply after they were placed from the track onto the heating table and is stabilized for the whole process. The solar cells are removed by the rail system after the pre-defined treatment time and are transferred into the unloading chamber. There, the samples are either collected manually or by a Bernoulli gripper. The cool down rate to the ambient temperature of the unloading chamber is 4.1 °C/s. For the dark annealing, the heating table temperature is slightly raised to 200 °C in order to obtain the same process temperature (the blue dash line). This measurement is repeated multiple times using similar but distinct solar cells, and the results did not deviate more than ~ 3% as shown in figure A.3.
The annealing process in the following content has a temperature profile similar to the red solid curve shown in figure 4.3, if not further specified.

5 Results – Influences of intensive light soaking on SHJ solar cells

In the following chapter, the experimental results are stated. The process parameters are investigated such as the duration, temperature, and intensity of the illumination to obtain insight into the light soaking mechanics. The process parameters are fixed to the parameters of the maximized gain. Afterwards, the light soaking influence on the passivation of symmetrical (i)a-Si:H/c-Si/(i)a-Si:H samples are investigated by QSSPC measurements. Besides, the charge carrier transport properties are investigated by measuring the contact resistivity between the ITO/a-Si:H layers. The sheet resistance of the ITO itself and the conductive properties of the doped a-Si:H layers are discussed.

5.1 Effect of process parameters on solar-cell performance

The parameters which potentially have an impact on the solar cells' efficiency are the duration, the intensity, and the temperature of the light soaking. Since the intensity and the temperature cannot be completely decoupled, their effects can not be completely separated. As described in chapter 3.7, the temperature can be set by the heating table and the intensity of the light separately. Additionally, air cooling can be applied to maintain a process temperature, which is limited to 100 °C-300 °C at 55 kW/m². For all experiments the compared solar cells were chosen from batches of similar efficiency and since the light soaking tends to affect the V_{OC} and FF, the cells were split into groups by equal η and product of $V_{OC} \times FF$ to avoid sample bias.

To observe the temperature influence, the treatment time was fixed to 90 s with an intensity of 55 kW/m². The process temperature was varied by changing the heating table temperature and using, if necessarily, the air cooling. In figure 5.1, the solar cell results obtained from the $J(V)$ measurements for process temperatures from 150 °C to 250 °C are shown in terms of absolute differences before and after the light soaking. The temperature of the solar cell was measured using the pyrometer, obtaining the real temperature from the calibration as described in chapter 4. The highest difference in efficiency $\Delta\eta$ is visible at higher temperatures of around 210 °C and is $\sim 0.45\,\%_{abs}$ with a spread from $0.3\,\%_{abs}$ to $0.6\,\%_{abs}$ as shown in figure 5.1 a). For lower temperatures at 190 °C the efficiency gain is $\sim 0.4\,\%_{abs}$ and for higher temperatures

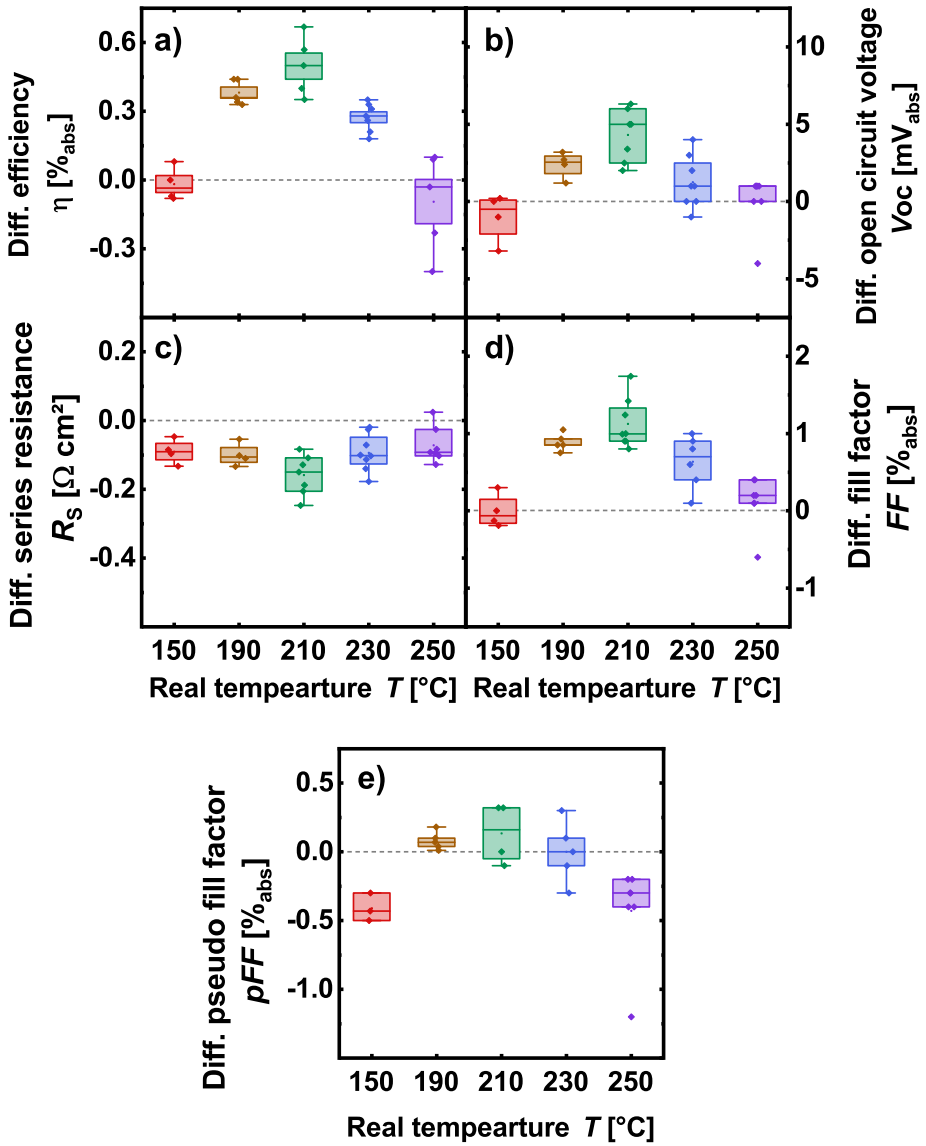

Figure 5.1: Influence of temperature present during light soaking. Shown are the absolute difference before and after light soaking for the η, V_{OC}, R_S, FF, and pFF in a) to e). The temperature is measured by the pyrometer and recalculated as described in chapter 4.2.

of 230 °C $\Delta\eta \approx 0.3\,\%_{abs}$. The differences in V_{OC}, FF and pFF show similar behaviour as indicated in figure 5.1 b), d) and e) respectively. For temperatures at 150 °C no improvement in η is visible. The gain property is lost at temperatures as high a 250 °C; this can be attributed to a too high process temperature. This missing gain or even loss is associated with the missing V_{OC} improvement and only a slight FF change. The R_S is reduced for all treatment temperatures, while showing a maximum decrease for at 210 °C of ~ $0.2\,\Omega cm^2$. The J_{SC} did not show a mentionable variation for different treatment temperatures. Temperatures higher than 150 °C are most likely

to have a beneficial influence on the solar cell, while temperatures above 230 °C can lead to an efficiency loss. A detailed discussion of the observed V_{OC} and FF changes is stated in chapter 5.3.

Obtaining an insight of the dependency of the illumination intensities, solar cells with a similar V_{OC}×FF product are treated with chosen illumination intensities while maintaining the temperature constant. The light intensity was set to 20 kW/m², 35 kW/m² and 55 kW/m² respectively. The heating table temperature was adjusted accordingly to keep the resulting process temperature of the solar cell constant at 210 °C to avoid influences of temperature changes. The relative change of solar cell $J(V)$-parameters before and after light soaking are shown in figure 5.2. The highest efficiency gain is observed for the highest illumination intensity of 55 kW/m². The J_{SC} remains constant for all treatments. The V_{OC} and the FF increase is the largest for 55 kW/m².

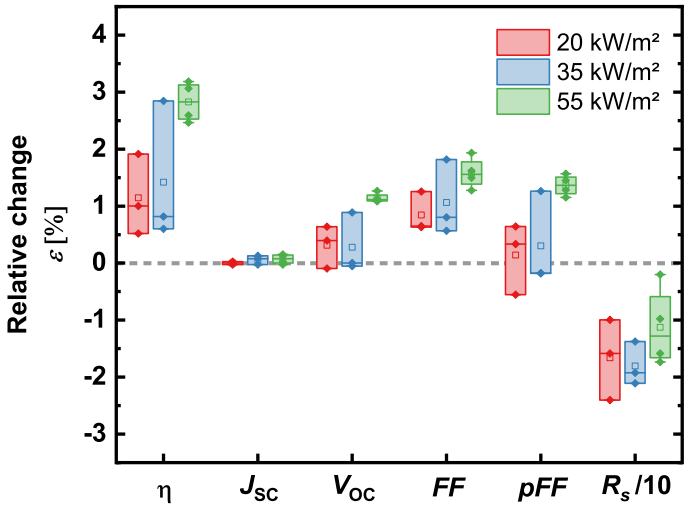

Figure 5.2: The relative change for the $J(V)$-parameters is shown for solar cells illuminated under different input intensities of 20 kW/m², 35 kW/m² and 55 kW/m² respectively. During all processes, the temperature of the heating table was regulated to obtain a constant process temperature of 210 °C of the solar cell during illumination. To keep the graphic clear, the relative change in R_S was divided by 10.

For lower intensities, the pFF only changes slightly, but shows a stable improvement for the observed solar cells illuminated at 55kW/m². The R_S decreases similarly for all illumination intensities. Therefore, a higher intensity is favourable for an efficient light soaking process. To obtain an insight into the duration needed to saturate the light soaking, the treatment time was varied. A batch of SHJ solar cells are exposed to accumulated light soaking under 55 kW/m² at 210 °C. The results are shown in figure 5.3. The efficiency gain already saturates between 40 s and 120 s of light soaking. The mean V_{OC} increases from 734 mV during the whole period of 570 s to 737.5 mV.

The largest change in V_{OC} is observed after the first treatment and possibly does not fully saturate over the 570 s of treatment time. The FF saturates similar to the efficiency and on these cells the pFF maintained constant over the whole treatment time. No substantial change in J_{SC} observed. The series resistance decreases already after nearly 20 s with the largest decrease after 5 s.

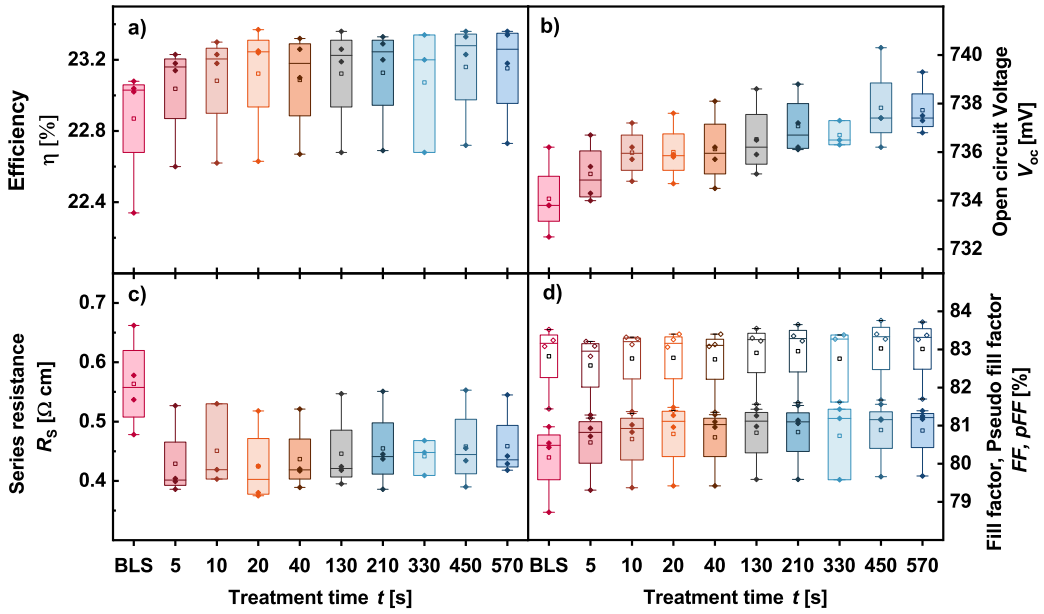

Figure 5.3: Absolute values of solar cell $J(V)$-parameters measured before (BLS) and after various accumulated light soaking times. The η, V_{OC}, R_S, FF, and pFF are shown in a)-d). In d) the filled boxes represent the FF and open boxes the pFF.

From the measurement, it can be concluded that the efficiency gain is related to a change in V_{OC} and FF similar to as observed by various other groups [18–20]. Concluding the temperature, intensity, and duration variations, the highest efficiency gain was observed for processes with 55kW/m² at 210 °C for processes. The saturation of the light soaking process is reached fast and for further treatments it will be set to 90 s. These process parameters will be set as the baseline receipt for the following thesis.

5.2 Influence of sample preparation

To obtain high passivation quality, a Hydrogen Plasma pre-Treatment (HPT) is carried out to flush the surface with hydrogen and set the growing parameter of the solar cell [65]. Two types of rear-emitter SHJ solar cells are prepared and their $J(V)$-characteristics evolution before and after light soaking is compared, as shown in figure 5.4. The light was illuminated on the n-side of all the cells for 90 s with an input intensity of 55kW/m² and a process temperature of 210 °C.

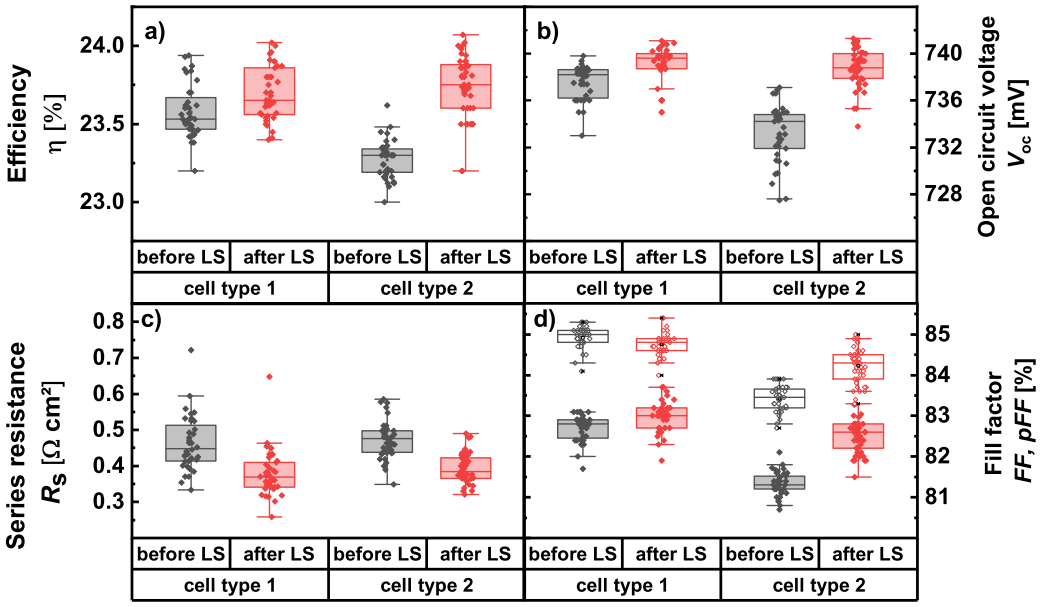

Figure 5.4: Measured (a) η, (b) VOC, (c) R_S, (d) FF (filled boxes) and pFF (empty boxes) of two types SHJ solar cells before and after light soaking. The values are based on more than 20 M2+ industrial-sized solar cells per batch. The light was incident from (n)a-Si:H side.

The difference between the two cell types comes from the sequence before p-side (i)a-Si:H deposition, where "cell type1" has a hydrogen pretreatment on the c-Si surface and "cell type2" has no such step, as explained in chapter 3.1. This different deposition strategy results in a different passivation effect, as can be seen from the initial V_{OC} and pFF values as shown in figure 5.4 b) and d). The FF difference of the as prepared cells comes from the pFF only since the R_S is almost the same for both types, as shown in figure 5.4 c). Consequently, the initial average efficiency of "cell type 1" is higher than that of "cell type 2" as shown in figure 5.4 a).

After light soaking treatment, the efficiency of "cell type 2" reaches a significant average improvement of up to 0.6% in absolute, which has overtaken that of "cell type 1" where only 0.2% gain in absolute is achieved. The efficiency gain is driven by the V_{OC} and FF improvement for both cell types, while no statistically significant changes are observed in the J_{SC} as displayed in figure A.4. A larger increase in V_{OC} is found for "cell type 2" compared to "cell type 1". The R_S decreases by the same magnitude for all the cells, this carrier transport enhancement will be discussed in detail in the following chapter. It is worth to note that the source for the greater increase in FF of "cell type 2" not only originates from the reduction in R_S, but also from the significant improvement in pFF, which is not the case for "cell type 1". This could be attributed to the surface passivation modification during light soaking and will be discussed in the next chapter.
It can be concluded that the effect of light soaking on solar cell performance is highly

dependent on the processing conditions of the solar cells. However, the gain of magnitude is related to initial states, especially for FF which is strongly influenced by both recombination currents and ohmic resistances. Interestingly, for both types of cells, annealing can bring the R_S down to the same level as light soaking, the post light soaking process on annealed cells can't reduce the R_S further. In the following only "cell type 2" solar cells will be regarded in the discussion since it shows a more pronounced light soaking effect.

5.3 Detailed analyses of light soaking

In the SHJ solar cells, a front n-side and a rear a p-side is prominent. Since the c-Si absorber will absorb nearly all the light, only the side facing the LED panel will be illuminated during the light soaking. Therefore, the influence of the illuminated side is investigated to obtain information about the influence of the absorption happening in the thin a-Si:H layers. Solar cells from "cell type 2" are prepared and divided into three groups. One group is illuminated from the front side (n-side) and one from the rear side (p-side) each for 90 s. This measurement is compared with a set of cells which are treated with a half light soaking treatment, each 45 s on either side, first from the p-side, then from the n-side.
Figure 5.5 illustrates the changes in efficiency of the SHJ solar cells using light soaking with two different light incident directions, one from the (n)a-Si:H side (n-side illuminated), the other from the (p)a-Si:H side (p-side illuminated). The results are shown in figure 5.5.

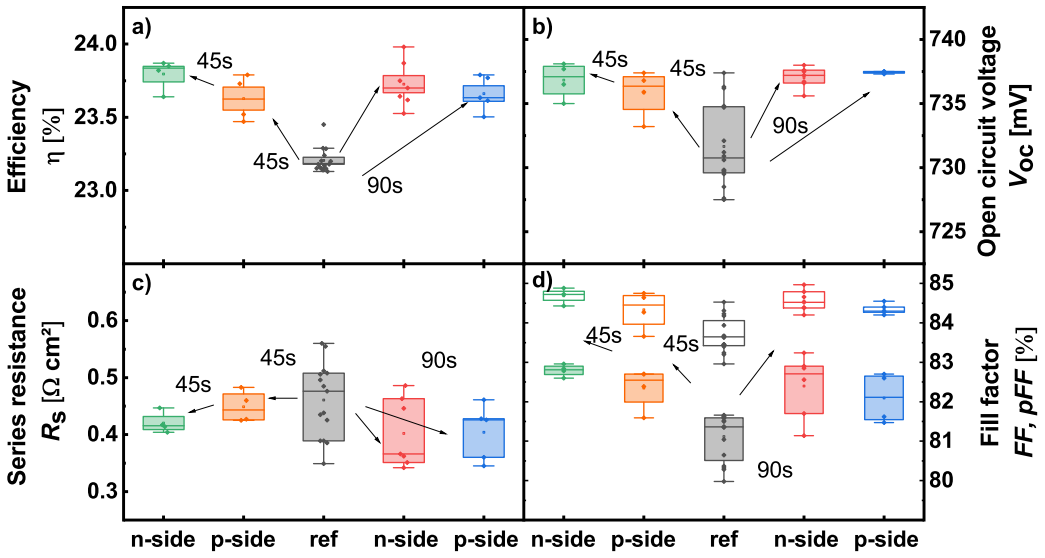

Figure 5.5: The absolute parameters before (ref) and after a light soaking form the corresponding illumination side is shown for a) η, b) V_{OC}, c) R_S, and d) FF (filled boxes) and pFF (empty boxes).

From the $J(V)$-parameters, an increase of η of ~ $0.6\%_{abs}$ for each group is visible. This

enhancement is driven by the change of V_{OC} and FF. The pFF increases similarly as the FF and the R_S is decreased after each treatment. From these measurements, two things can be observed. Firstly, after the first treatment, roughly 75 % of the improvement is obtained, and after the second about 25 %. The two treatments for 45 s result in a similar improvement as one 90 s. The second observation is that the improvement is independent of the illumination side. It can be seen that the light soaking effect does not show a dependence of the illumination side, therefore is not origin from the illumination of the a-Si:H.
As already discussed in the previous results, the light used here will be absorbed in the first several micrometers of the solar cells, the identical behaviour observed suggests that the performance improvement cannot be caused by absorption of light photons in the hole or electron contact. This correlates well with reports by Kobayashi et al., indicating that the performance increase in SHJ solar cells is driven by carrier injection from the absorption of light photons in the wafer bulk [19].
Since the improvement takes place in V_{OC} and pFF, it can be attributed to a change in passivation which will be discussed in the next chapter.

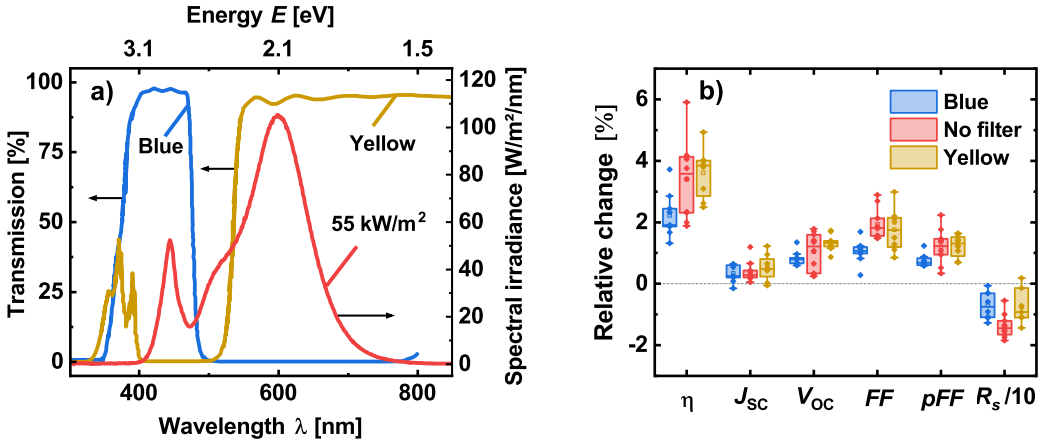

Figure 5.6: The transmission spectrum of the filters and spectrum of the LiSO is shown in a). The relative changes of the solar cells $J(V)$-parameters are shown in b). To keep the graphic clear, the relative change in R_S was divided by 10.

It can be speculated that the light soaking is independent of the photons' energy, as long as they are absorbed in the bulk since high energy photons will be mainly absorbed in the ITO and a-Si:H layers. To test this hypothesis and to investigate if one of the given wavelengths is responsible for the change during light soaking, custom test samples on 78 mm x 78 mm wafers are produced. The LiSO spectrum shows two main peaks at 450 nm and 600 nm as discussed in chapter 4. Two different filters are placed on top of the solar cells to block either the 450 nm or the 600 nm peak. The transmission of the filters and the given spectrum are shown in figure 5.6 a).

The relative change of $J(V)$-parameters of the solar cell after the treatment are shown

in figure 5.6 b). All treated solar cells gained in between 1 %$_{rel.}$ – 6 %$_{rel.}$ in efficiency. Due to the large spread and the small sample size, it is difficult to obtain a conclusion. However, it can be concluded the "Blue" filter, which blocks most of the spectrum, has a slightly lower improvement compared to the other treatments. This can be attributed to the lower intensity reaching the solar cell rather than the higher energy inserted by the photons. The solar cells covered with the "Yellow" filter also show a lower improvement compared to the ones illuminated with the full spectrum. Therefore, the light soaking effect cannot be attributed to the present high energy photons and is more likely induced through the presence of induced charge carriers. This correlates well with previous results obtained by illuminating the solar cell from different sides. Result from Kobayashi et al. and Cattin et al. indicate that the performance increase in SHJ solar cells is driven by carrier injection from either the absorption of photons or through injected charge carriers in the wafer bulk by a reversed bias [19, 22] and correlate well with presented results.

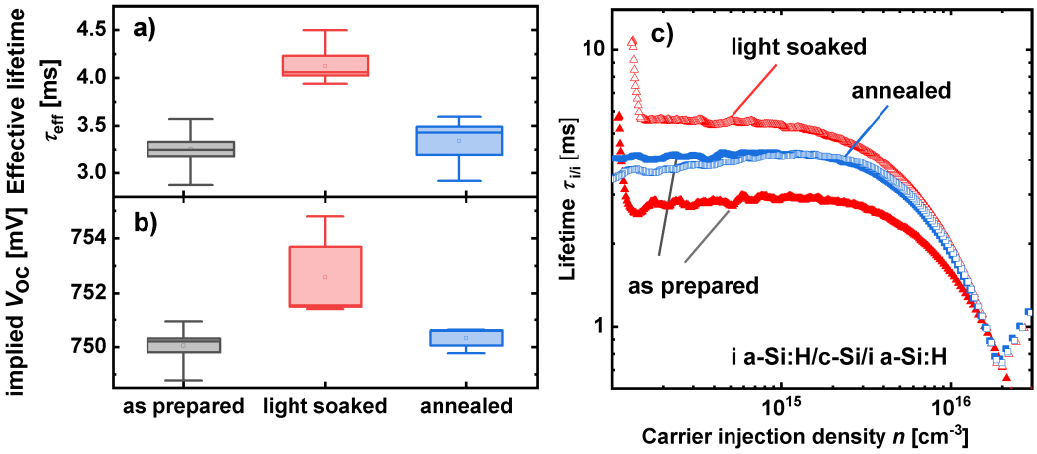

Figure 5.7: In a) the τ_{eff} and in b) the iV_{OC} of i/i samples after light soaking and after annealing is shown. In c) the τ_{eff} versus n is shown for the i/i passivation samples before (filled symbols) and after (empty symbols) light soaking (red triangles) and annealing (blue squares).

The carrier injection effect would mainly influence the passivation of the cells which has an impact on the V_{OC} enhancement. To further verify this symmetric structure of p-side (i)a-Si:H passivated crystalline silicon (i) a-Si:H/c-Si/(i) a-Si:H (i/i) samples were prepared, and the injection-dependent effective minority carrier lifetimes (τ_{eff}) were measured before and after light soaking as well as a dark annealing for 90 s at 210 °C. The doped layers were omitted in the samples to avoid the influence from electric field effect. The symmetrical i/i passivation samples are prepared with a 7 nm thin (i) a-Si:H layer deposited by PECVD with the same recipe on both sides, omitting the HPT. Each group consists of 5 samples. In figure 5.7 a) the τ_{eff} at n = 10^{15} cm^{-3} measured by QSSPC before and after treatment is shown. The mean τ_{eff} increases from ~ 3.25 ms to ~ 4.1 ms after the light soaking, while remaining at

~ 3.4 ms after the annealing. In figure 5.7 b) the corresponding iV_{OC} obtain at 1-sun conditions shows an increase of ~ 3 mV after light soaking while remaining constant after annealing. In figure 5.7 c) one example curve of the τ_{eff} versus the n for the annealing and light soaking treatment is shown.

This result indicates that the passivation increase is caused by carrier injection induced from illumination, which is identical like the observation under forward-voltage bias in the absence of illumination [18]. The injected carriers diffuse through the wafer and recombine at the a-Si:H/c-Si interface, the liberated energy from such recombination may aid in nearby interface-state healing and improve the passivation.
This light induced carrier injection effect is more effective for the case of relatively poor initial passivation [21]. In the case of a well-passivated interface, the healing benefit from recombination of carriers may be less or compensated by the defects induced in the a-Si:H bulk from the charge injection [66]. This eventually results in no significant lifetime improvement or even a lifetime degradation [18].

After the annealing, a change in the low injection region is observable as shown in figure 5.7 c), which is typically attributed to a change in the charge induced in the c-Si surface space-charge region. This suggests that the degradation effect is related to a change at the outer surface of the (i)a-Si:H layer, like e.g., post-oxidation or possibly water adsorption, leading to a change of the outer surface potential. This degradation is shown to appear over time if the sample is stored in dark under ambient air condition [67]. The origin remains unclear and needs further investigation. The results suggest that light soaking has a beneficial effect on the effective lifetime, while under annealing the lifetime only slightly changes.

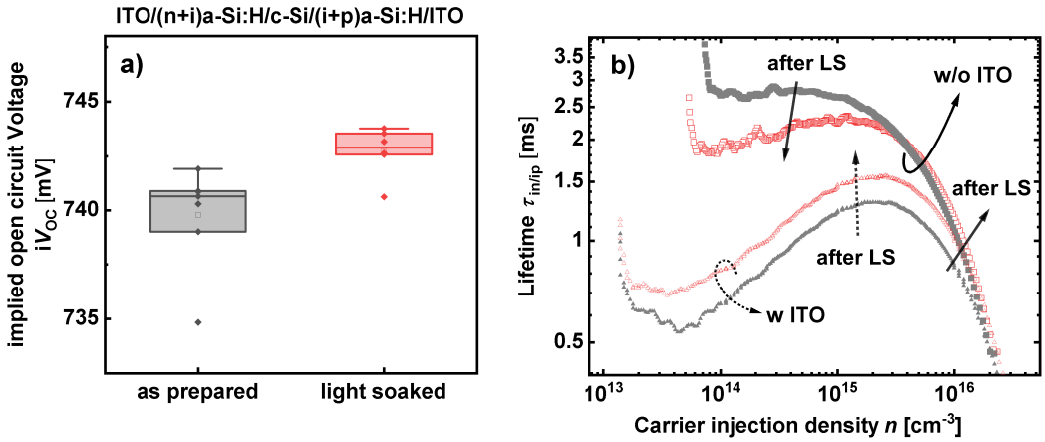

Figure 5.8: In a) the iV_{OC} for in/ip samples with ITO are shown before and after light soaking. In b) effective lifetime versus the carrier injection density is shown for in/ip samples with and without ITO before and after light soaking.

To investigate the influence of light soaking with the presence of doped layers, solar cell structures of (n+i)a-Si:H/c-Si/(i+p)a-Si:H (in/ip) are prepared. These in/ip samples were prepared for the investigation on the real device. It is already known that TCO sputtering can result in sputter damages, which should be cured out by the screen printing annealing [52]. The iV_{OC} at 1-sun injection conditions is shown in figure 5.8 a) before and after the light soaking treatment. It increases from 740 mV to 743 mV similar to the i/i samples. The difference of iV_{OC} to V_{OC} is a measure of the contact's selectivity, with iV_{OC} - V_{OC} = 0 representing perfect contact selectivity. Since the observed increase in V_{OC} after light soaking is 6 mV the contact selectivity may be increased after light soaking.

In figure 5.8 b) the $\tau_{eff}(n)$ plot shows that for the in/ip without ITO the τ_{eff} in the region $n < 10^{15}\,cm^{-3}$ decreases. For samples with ITO the τ_{eff} is increased over the whole range by shifting the curve towards higher lifetimes, which is attributed to an increased chemical passivation. Branz et al. showed that the hydrogen motion in a-Si:H is field dependent due to presence of mobile charged hydrogen species [68]. Therefore, the hydrogen movement depends on the Fermi-level position in the a-Si:H and is influenced by the presence of doped a-Si:H layers [68]. Despite the fact, that the in/ip samples degrade during light soaking, which needs further investigation. Samples coated with ITO obtain an increase in chemical passivation which is comparable to the change observed for the i/i samples and is reflected in the observed the solar cells results. It should be noted that the presence of the conductive oxide does not affect the WCT instrument measurement procedure, since the calculations are based on photoconductance variations and not on its absolute value [69].

5.4 Quantification of the temperature effect during light soaking

In completion with the previous discussion of the carrier injection effect which is mainly influenced by the passivation of the solar cells, which has an impact on the V_{OC} enhancement, in the following the thermally dominated carrier transport variations will be investigated. A proper post thermal treatment could be beneficial for the passivation and carrier transport in SHJ solar cells [70, 71]. The temperature profile of both the annealing and the light soaking processes is shown in figure 4.3. The process conditions for and equivalent process to the light soaking process was measured and discussed in chapter 4.

To decouple the heat effect from the thermal assisted light soaking process, the annealing process which simulates the thermal profile in light soaking (the red solid line in figure 4.3) was applied on solar cells and compared to solar cells with a light soaking treatment. Figure 5.9 summarized the $J(V)$ information.
The annealed group shows an increase of efficiency of ~ 0.2 $\%_{abs}$. The light soaked

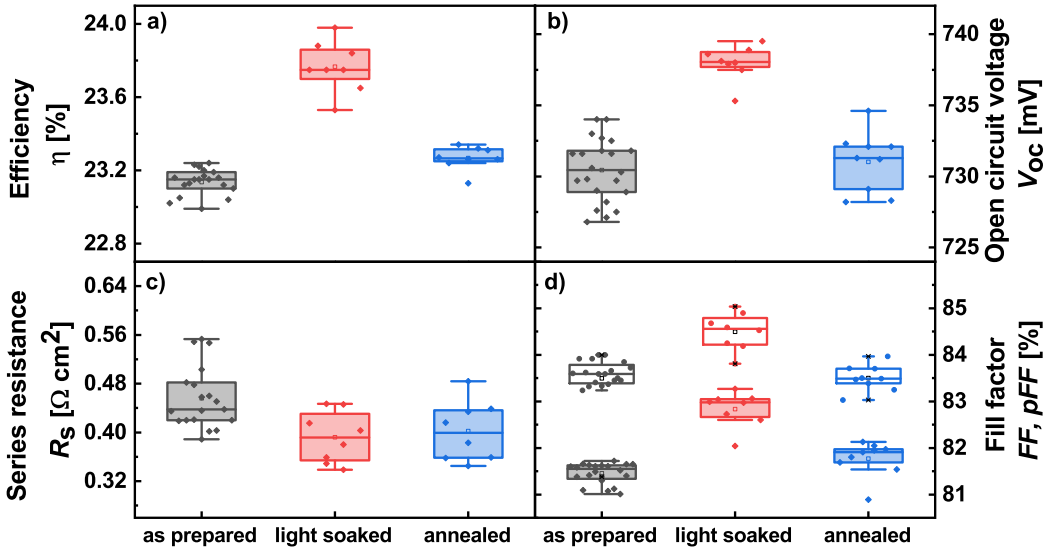

Figure 5.9: The results for solar cells either annealed or light soaked are shown. The η, V_{OC}, R_S, FF (filled boxes) and pFF (empty boxes) are shown in a) to d).

group has an increase of ~ 0.7 $\%_{abs}$. While the V_{OC} of the solar cells of the light soaked group increase, the V_{OC} of the annealed group shows no change. The FF of the light soaked groups changes from 81.5% to 83% while the pFF changes from 83.5% to 84.5%. No change in J_{SC} was observed. The annealed group shows a slight change in FF which could be completely attributed to the decrease in R_S because the pFF remains constant. Interestingly, both groups have a similar R_S decrease to the same level. This is a strong indication that the R_S drop of ~ 90 $m\Omega cm^2$ mainly comes from the thermal effect during the light soaking process, if the SHJ solar cells haven't undergone sufficient heat treatment before.

To further decouple the heat effect from the thermal assisted light soaking process, the annealing process which simulates the thermal profile in light soaking was applied on solar cells, then the cells were light soaked and compared with directly light soaked solar cells. The results are shown in the figure A.5 in the appendix, since the trend is the similar as shown in figure 5.9.

It can be concluded that annealing can bring the R_S down to the same level as light soaking, the post light soaking process on annealed cells can't reduce the R_S further. It is worth to mention that the maximum cell process temperature is not more than 200 °C, which is lower than the annealing temperature here. However, this short time annealing can't dramatically improve the V_{OC}. The illumination during light soaking should be responsible for the enhancement of V_{OC}. Meanwhile, this dramatic V_{OC} improvement is also the main reason of FF enhancement.

In a SHJ solar cell, the R_S can be very sensitive to the thin film layers in the contact stack. Since thin a-Si:H layers are used, their film properties, especially the conductivity, are always an important factor for achieving high FFs [72, 73]. If the contact

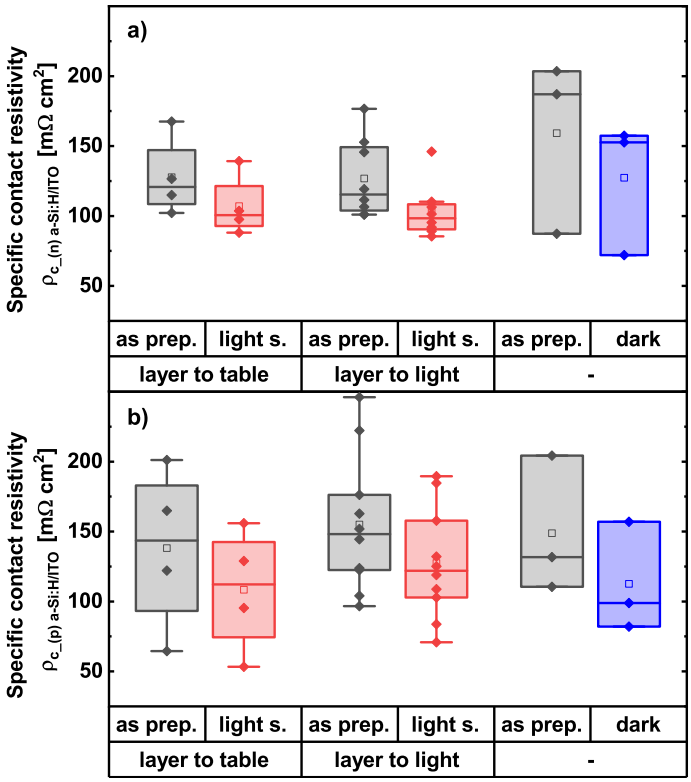

Figure 5.10: The $\rho_{(n)a\text{–}Si:H/TCO}$ in a) and the $\rho_{(p)a\text{–}Si:H/TCO}$ in b) for the as prepared (as prep.) state, after light soaking (light s.) and after dark annealing (dark) is shown.

improvement is only evoked by the thermal effect in light soaking process, this could mean that the light induced degradation of conductivity in thick a-Si:H films [72, 73] doesn't emerge in thin films. To reveal the implicit mechanisms, the TLM measurement was carried out to extract the vertical contact resistivity between TCO and n-side/p-side a-Si:H layers on both sides of the solar cells. The p-side a-Si:H stack was prepared like in "cell type 2" as a representative. Samples were split into groups with similar initial contact resistivity. To reveal the illumination and thermal induced effect, the pattern sides were exposed to light or table during the light soaking process, a group of samples with pure thermal treatment was also prepared for comparison.

The TLM is measured before and after light soaking and before and after a comparable heat treatment. In the light soaking group, one half is placed with the contacts layer facing the illumination source, while the other half is facing the heating table. The results are shown in figure 5.10.

As shown in figure 5.10 a) and b), the contact resistivity of the (n)a-Si:H/TCO contact is about, $\rho_{(n)a-Si:H/TCO} = 120\,m\Omega cm^2$ which is slightly lower than the (p)a-Si:H/TCO contact of $\rho_{(p)a-Si:H/TCO} = 150\,m\Omega cm^2$. The contact resistivity of the n-side is expected to be lower because of the lower (n)a-Si:H/c-Si band offset and the isotype ITO/(n)a-Si:H junction. The contact resistivity is reduced after light soaking, which can be attributed to the temperature effect, since the dark annealed samples show a similar behaviour. The contact resistivity of the n-side is lowered by approximately, $25\,m\Omega cm^2$ to, $\rho_{(n)a-Si:H/TCO} = 100\,m\Omega cm^2$ while the contact resistivity of the p-side is reduced by approximately $40\,m\Omega cm^2$ $\rho_{(p)a-Si:H/TCO} = 110\,m\Omega cm^2$. The average total R_S drop after cells with light soaking process is about $90\,m\Omega cm^2$, which means ~ 45% of the improvement comes from the cell p-side.

The samples with TLM patterns facing the heating table may have similar treatment conditions like the samples underwent a pure annealing, since the light will not penetrate the wafer to reach its back side. The results demonstrate that the R_S drop after light soaking is not induced by the absorption of light in the a-Si:H layers, which again reveals that enhanced carrier transport may be a thermal effect.

The dark conductivity of doped a-Si:H layers and the sheet resistance (R_{sh}) of ITO were further investigated to reveal the implicit mechanism of reduced contact resistance. Since the samples for conductivity measurement were prepared on Corning Eagle 2000 glass substrates whose thermal conductivity is much lower than silicon wafers [74, 75], the film sides were glued on a silicon wafer with conductive Ag paste to ensure a proper thermal conductance with the table during the light soaking. A detailed illustration is shown in figure 5.11. The glass substrate has >90% transmittance at the emission peaks of 450 nm and 600 nm [74], most of the light can penetrate through the glass to reach the film layers.

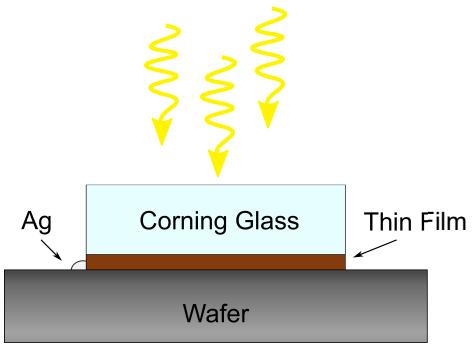

Figure 5.11: Illustration of thin film layer treatment during light soaking. The thin layer is partially glued on a wafer, which mimics the situation on SHJ solar cells.

The n-doped layers have a thickness of 29 nm and the p-doped layers of 155 nm measured by ellipsometry. The substrate temperature during deposition was 200 °C. The

samples undergo a treatment of either light soaking at 210 °C under 55 kW/m² for 90 s or dark annealing at similar conditions. After the corresponding treatment, 700 nm thick silver contacts are deposited on top by evaporation for the conductivity measurement. In figure 5.12 the results of the conductivity measurements are shown before and after the corresponding treatment.

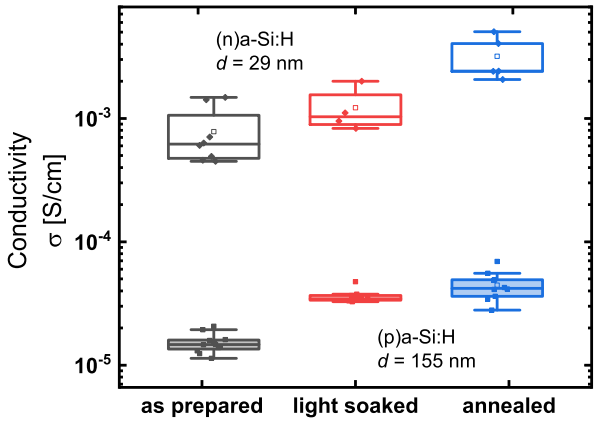

Figure 5.12: Conductivity of (n)a-Si:H and (p)a-Si:H before and after light soaking or dark annealing. The (p)a-Si:H increases in either way, while the (n)a-Si:H shows a SWE like response to light soaking.

In case of the (p)a-Si:H, the average dark conductivity increases from $1.51 \cdot 10^{-5}$ S/cm to $4.46 \cdot 10^{-5}$ S/cm after the annealing and to $3.61 \cdot 10^{-5}$ S/cm for the light soaked samples. The two processes seem to have similar impact on (p)a-Si:H. Since the conductivity of the (p)a-Si:H samples increases independent of the applied treatment, it can be attributed to a temperature effect. This increase could be explained by the increase of doping efficiency in (p)a-Si:H films due to the transfer of hydrogen from Si-H to B-H during light exposure [28]. For (n)a-Si:H, the average dark conductivity increases from $7.8 \cdot 10^{-4}$ S/cm to $3.19 \cdot 10^{-3}$ S/cm after the annealing and to $1.22 \cdot 10^{-3}$ S/cm after the light soaked samples, respectively. While the (p)a-Si:H does benefit from the annealing and the light soaking treatment, the (n)a-Si:H layer shows a light-induced degradation of conductivity compared to the annealed samples, similar to the reports of Staebler and Wronski in thicker a-Si:H layers [15]. Even while the (n)a-Si:H is not increased in conductivity, the $\rho_{(n)a-Si:H/TCO}$ is lowered after light soaking. When highly doped n-type a-Si:H layers are light soaked, the defect density may increase, compromising the thermal effect's enhancement of conductivity [15]. Since the TLM samples are treated after silver metallization, shading and reflection is more prominent and therefore the temperature effect dominated, while in the conductivity set up the whole layer is illuminated though the glass. Another difference is the structure of the TLM samples where ITO and the (i)a-Si:H layer are present.

To further investigate the changes in the R_S, 100 nm thick ITO layers were deposited on corning glass and the sheet resistance is measured by using the 4-point probe technique. The thickness was measured by ellipsometry. The samples undergo an annealing at 170 °C for 40 min as the solar cells for the metallization. The results before and after a light soaking and a corresponding annealing treatments are shown in figure 5.13. After each treatment, the mean R_{sh} is lowered by ~ 8 Ω/sq to a similar level, which is one of the responsible reasons for the increased carrier transport. These changes in ITO are beneficial for the cells R_S because the current transport is transferred to a lateral in the ITO, which lowers the effective R_S. As shown in figure 5.13, the R_{sh} of ITO reduces to a similar level, which is one of the responsible reasons for the increased carrier transport.

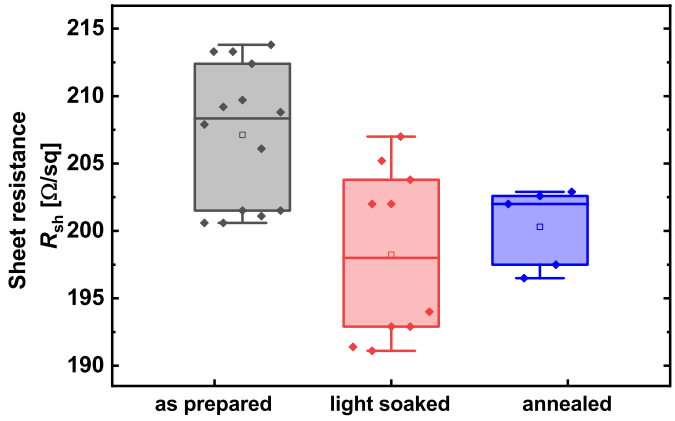

Figure 5.13: Sheet resistance R_{sh} obtained by 4-point-probe method measured on a 100 nm ITO on corning glass before and after an annealing or light soaking treatment. The R_{sh} is lowered by both treatments.

The measured R_{sh} obtain comparable high values. This phenomenon is already described by Haschke et al. It is observed that the R_{sh} obtained by 4-point-probe measurements of ITO on corning glass differs from vales obtained by TLM on crystalline wafer, which remains unexplained [76].
A further investigation on active carrier concentration of (p)a-Si:H and (n)a-Si:H layers fabricated on 280 µm wafer substrates was conducted by ECV. Increased doping is expected to decrease the contact resistivity, as simulated and experiments shows [70, 77]. The conductivity measurement reveals a change in the conducting properties of the a-Si:H. Layers prepared in the same process as PECVD as the conductivity samples were deposited on polished float zone (FZ) wafers. The wafer is cut into 10 mm×10 mm pieces and treated in the same processes as the conductivity samples. Several samples were glued with conductive silver paste onto a carrier wafer. The layer side was either facing the illumination source or the heating table. The active

carrier concentration is measured by ECV and the results are shown in figure 5.14.

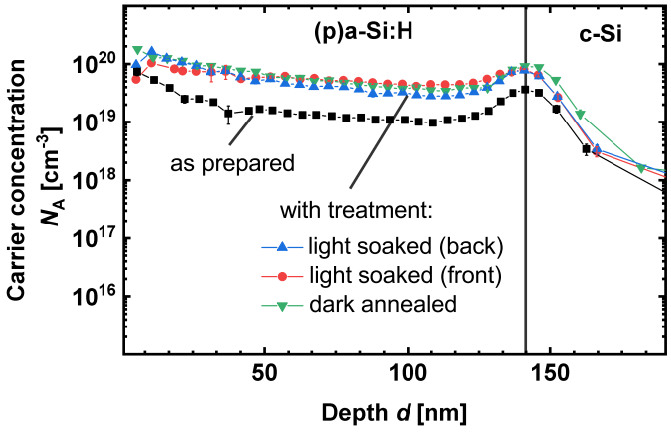

Figure 5.14: ECV measurements of thin p-layers on polished FZ wafers. The carrier concentration N_A versus the depth d of a (p)a-Si:H layer is shown for various treatments.

The peak active carrier concentration changes in the (p)a-Si:H from $\sim 3 \cdot 10^{-19}\,\mathrm{cm}^{-3}$ to $\sim 9 \cdot 10^{-19}\,\mathrm{cm}^{-3}$. This increase in active carrier concentration is observed for either a light soaking treatment as well as for the annealing. Neither the sample processing (light soaking or annealing) nor light incident direction has a different impact on the active carrier concentration. The same gain compared to as prepared (p)a-Si:H confirms the negligible effects of light on doping efficiency enhancement. Recently, Liu et al. reported the light-induced activation of boron doping in (p)a-Si:H could increase the charge carrier transport in SHJ solar cells [29]. As discussed, this is not the situation in this thermal assisted light soaking process, where the thermal effect still dominates the variation in carrier transport. The results for the (n)a-Si:H layers are shown in figure A.6, the change in active dopant concentration is not clearly observed neither for light soaking nor annealing.

It can be concluded that during the temperature assisted light soaking the R_S decrease can be attributed to a temperature effect which decreases the contact resistivity of both contacts. Since no V_{OC} increase after the annealing is visible, the increase in the p-layer effective doping and therefore the possible increase in V_{bi} is not directly transferred to the V_{OC}. The change in FF during annealing can be explained by a decrease of the height of the Schottky barrier on the (p)a-Si:H side, leading to the increase of the probability of hole tunnelling. This improves the hole transport [78]. Adjusting the work function mismatch of the (p)a-Si:H and the ITO layer can be reached by increasing the net doping [79].
This increased doping leads to an improved selectivity and an increase in FF as observed by samples prepared with different doping densities [80].

In the previous chapter, a change in the passivation and conductivity properties of the a-Si:H was observed, which could be related to hydrogen movement and/ or effusion during light soaking. To quantify this movement, SIMS measurements were carried out. The SIMS measurements of a ~ 40 nm thick (p)a-Si:H is shown in figure 5.15. For

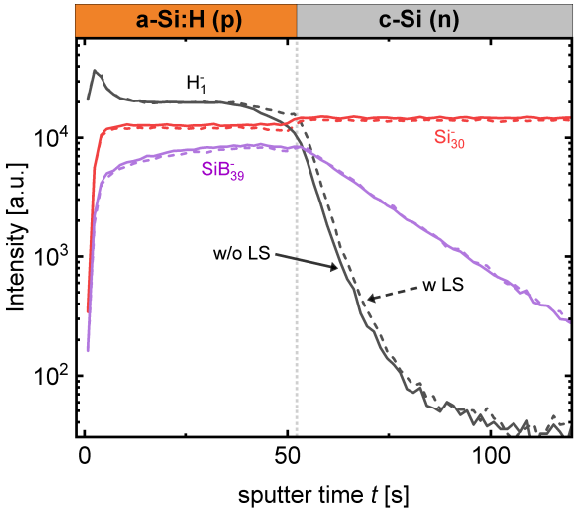

Figure 5.15: Silicon, hydrogen, and silicon-boron SIMS depth profiles of (p)a-Si:H as deposited (w/o LS) and after light soaking (w LS).

the processes temperatures of 210 °C at 90 s, no significant movement of hydrogen is observed in the samples after light soaking. Besides the hydrogen, no boron diffusion is observed during the light soaking. For higher temperatures, H_2 diffusion can be obtained, which will take place mainly in the p-layer [68]. It was observed by Cruz et al. that for higher temperatures the H_2 can diffuse into the ITO [81], which has to be further investigated but is not observed in the presented samples. Veriman et al. concluded the role of hydrogen motion is still unclear [82] contradicting to other reports by Liu et al. [29]. To further quantify the involvement of H_2 in the conductivity and passivation changes, effusion measurements were carried out on symmetrical i/i, ip/ip and p/p layers deposited on 280 µm FZ wafers. The results are shown in figure A.7 and unfortunately no change between the as prepared and light soaked samples is observed.

5.5 Stability of the light soaking effect in SHJ solar cells

For several reasons, it is interesting if the efficiency gain obtained by light soaking does hold over time. A group of solar cells are light soaked at 210 °C for 90 s under 55 kW/m^2 and are measured regularly. A reference group from the same batch were measured at the same times. Both groups were stored in the dark between the measurements in air under ambient conditions. The results are shown in figure 5.16

and the $J(V)$-parameters are summarized in figure 5.17. The light soaking show the similar trend as already observed and discussed in detail in earlier chapters. The solar cells were measured over a period of 217 days. The group which undergo a treatment show an improvement after light soaking, which is maintained over the whole period. A similar degradation can be observed in both groups. The degradation over time is driven by a change in V_{OC} and FF. The pFF remains constant for both groups and both groups show an increase in R_S.

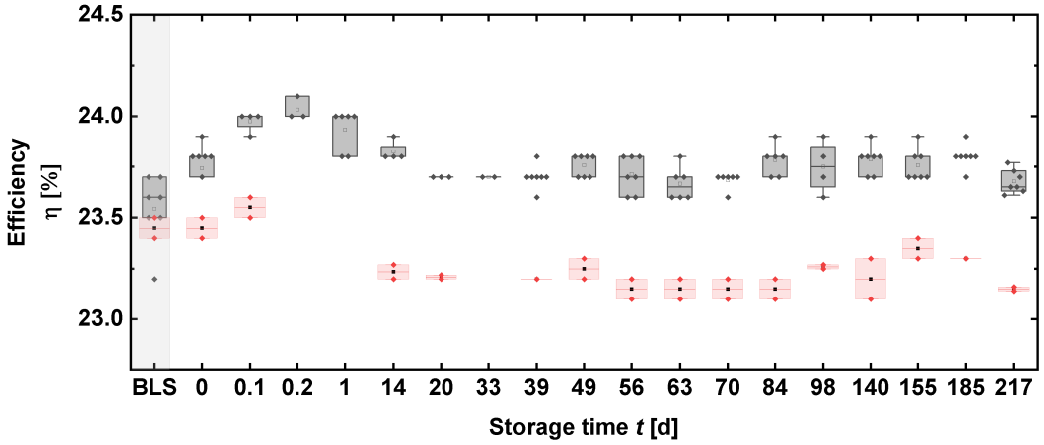

Figure 5.16: Stability of the light soaking effect measured over a period of 217 days. "BLS" stands for the initial state before light soaking.

Degradation of the cell can be related to a passivation loss over the time, even with the ITO capping layer [67]. It can be speculated that the origin of the R_S could be due to the multiple testing. Through the multiple measurements the contact fingers can be damaged in the region of the busbars which is visible for both groups. Cattin et al. observed a degradation in their structure a light soaking effect they could confirm, that this effect stays stable over the period of 4 months [22]. Contrarily to light-induced degradation of a-Si:H thin-film solar cells, the light-induced improvement of SHJ devices is stable.

5.6 Further heat treatments on light soaked solar cells

A major concern is the stability and reversibility of the light soaking effect. The behaviour of the cells' performance of alternative heat and light soaking treatments is investigated. A group of solar cells underwent a light soaking (LS) treatment with 55 kW/m^2 at 210 °C for 90 s and a subsequent heat treatment (dAN) of 200 °C for 90 s afterwards. The solar cells results are shown in figure 5.18 a)-h). The mean value of the efficiency gains 0.8 $\%_{abs}$ after the first light soaking. As already discussed, this can be reached by a gain of V_{OC} of 8 mV and a FF of 1.5 $\%_{abs}$. At the same time, the pFF changes ~ 1 $\%_{abs}$ and the R_S decreases while the J_{SC} remains nearly constant. Afterwards the first dark annealing (dAN) the effect is partially set back resulting

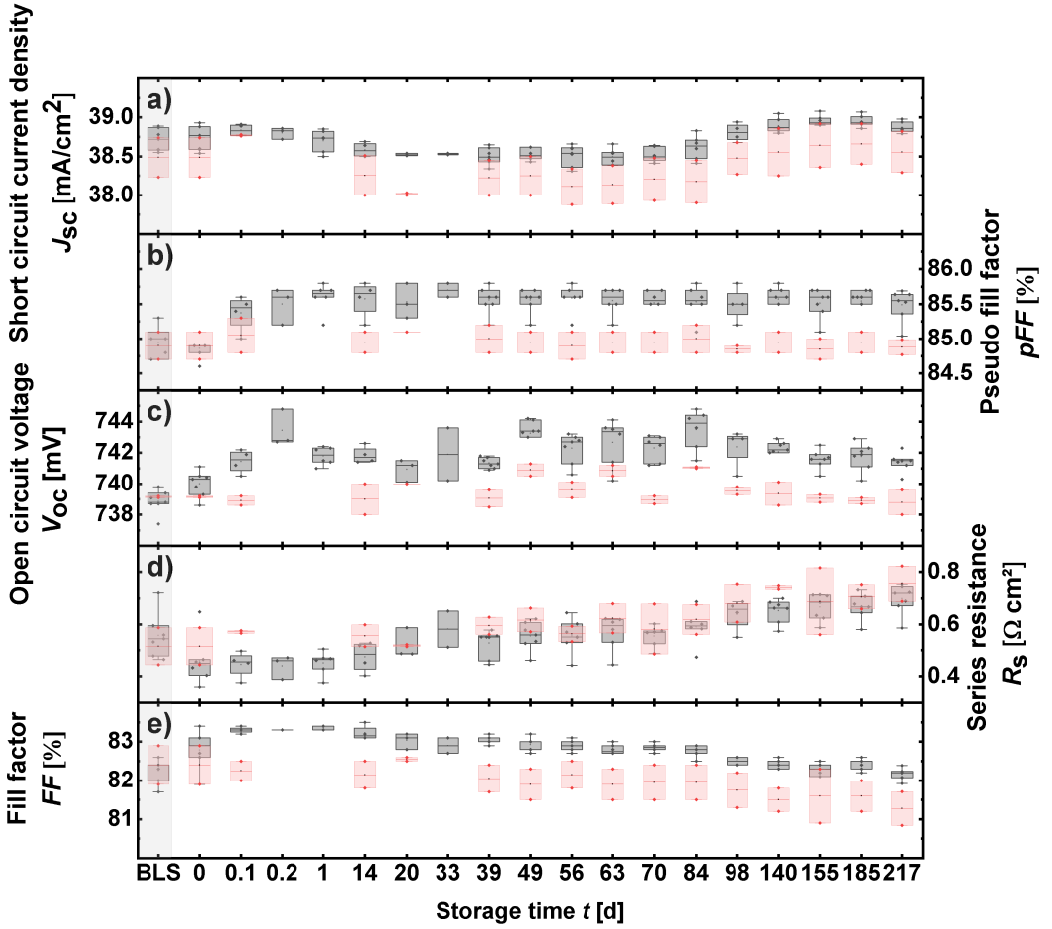

Figure 5.17: $J(V)$-parameters showing the stability of the light soaking effect, measured over a period of 217 days. "BLS" stands for the initial state before light soaking.

in a lower η which is still 0.3 $\%_{abs}$ higher than the initial η. After a second light soaking (2LS) the efficiency increases again but to a slight lower values as the first light soaking. After the next consequent annealing (2dAN) and light soaking (3LS) treatments, the trend continues. Analogue to the η a similar variation in V_{OC}, FF and pFF is visible. The R_S is only decreased after the first treatment. Despite the large scatter of R_S values a slight variation is observed after each annealing and light soaking.

This observation is in agreement with reports form Kobayashi et al. where the light soaking benefits were stable upon annealing [18] and contrasts with the studies of Bao et al. where the light soaking is almost fully reversible [20]. This activation and deactivation of the light soaking show that the changes induced by carrier injection are partially reversible with temperature. Tentatively, it could be speculated that the change in V_{OC} and pFF could be explained by a pool of defects, passivated by mobile hydrogen ions during light soaking, and following a distribution of thermal annealing

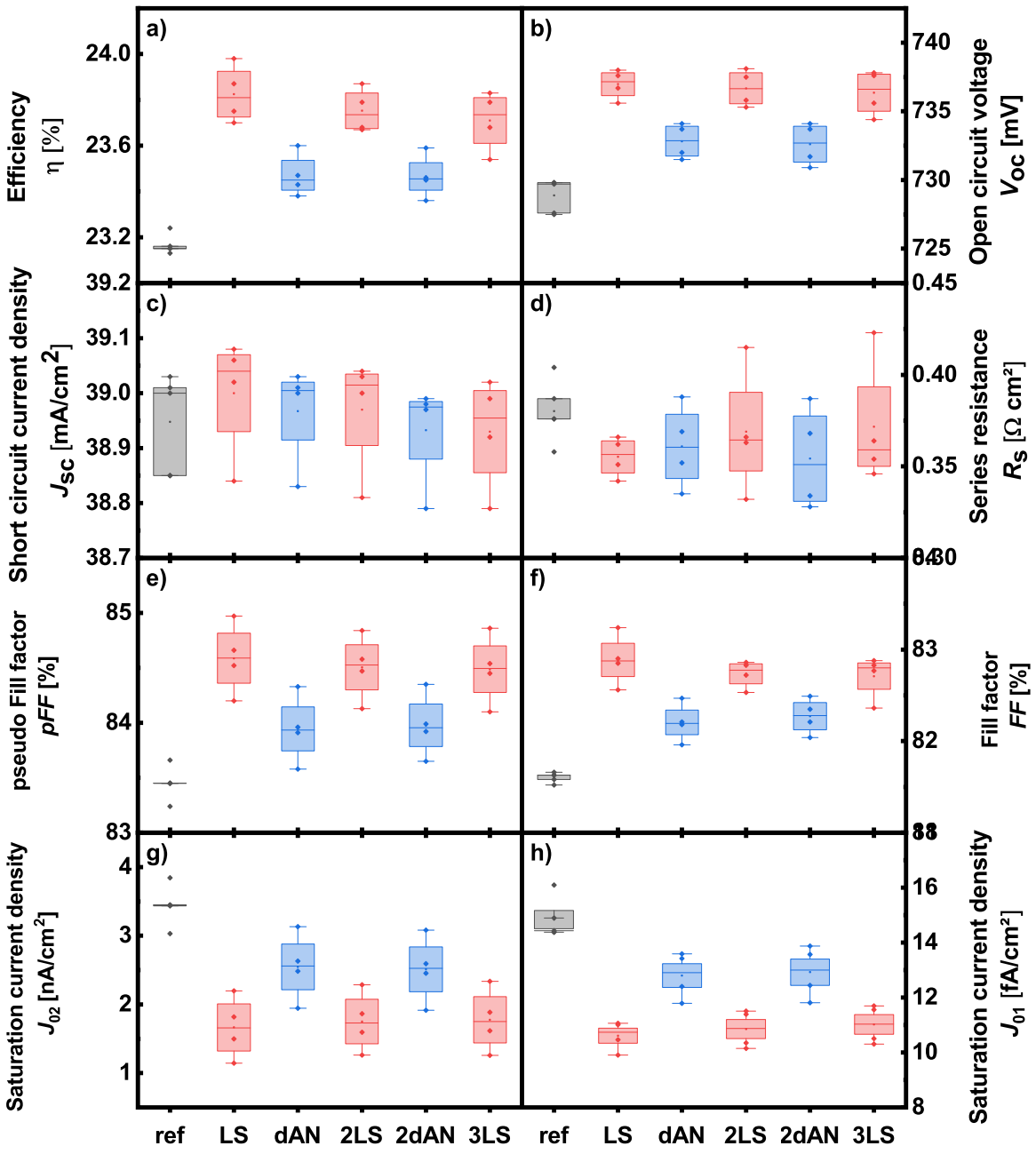

Figure 5.18: $J(V)$-parameters of solar cells, η, V_{OC}, J_{SC}, R_S, pFF, FF, J_{02} and J_{01} are shown in a) to h) for the initial state (ref), after repeated light soaking (LS) and after a heat treatment at 210 °C for 90 s (dAN).

energies, similarly to light-induced defects in a-Si:H [83]. Bao et al. attributed the decreasing trend after 4 cycles to the loss of repeating testing and contacting [20]. Hata et al. showed that light induced changes in a-Si:H are fully reversible by annealing for 1 hour at 220 °C [84], permanent light induced structural changes are reported by Stutzmann et al. remaining in irreversible changes after multiple light soaking-annealing cycles [27]. The behaviour of the R_S which seems to saturate after the initial treatment, and only a small variation after each treatment is observed. Due to the comparable large spread in the R_S further investigation is needed.

6 Transferability of light soaking effect to SHJ modules

In the following chapter, a module will be refereed as a single solar cell encapsulated in a front and back sheet encapsulation. In the real application, a module is a collection of more cells which are soldered in series and in parallel strings by an interconnection. The interaction of solar cells will be neglected, and it will be concentrated on the light soaking effect on a single encapsulated solar cell. To investigate if the light soaking treatment is transferable to modules, first the impact of the encapsulation process on the light soaking gain has to be quantified. In the second section, a process applicable on modules is developed. This is necessary since the encapsulation materials have a comparable low melting point.

It will be concentrated on the behaviour of the light soaking on the solar cell before and after the lamination, and interconnection issues will be neglected by using only one encapsulated solar cell. It was found that TPO encapsulated solar cells improve their efficiency over 2000 h of light soaking at 1-sun [56], therefore and for the sake of clearness the response of TPO encapsulated cell will be investigated.

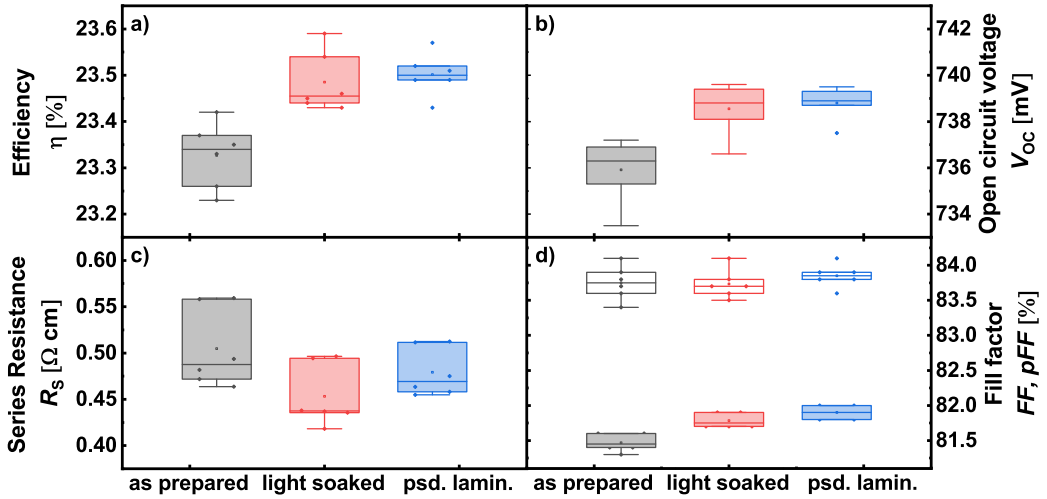

Figure 6.1: Solar cell parameters of consequent light soaking and pseudo lamination process a) η, b) V_{OC}, c) R_S, d) FF (filled boxes) and pFF (empty boxes).

6.1 Effect of temperature during the lamination process on light soaked SHJ solar cells

As described in chapter 3.2 the encapsulation is performed under low temperature as 125 °C for 16 min to obtain a good connection of the solar cell. This process used at the IEK-5 was optimized in previous works. To observe the temperature influence of the lamination on the light soaking effect, solar cells are prepared and undergo an equivalent heat treatment refereed as "pseudo lamination". In figure 6.1 the $J(V)$ characteristics of the solar cells after successive treatments are shown. The efficiency of the solar cell increases after light soaking, as already discussed in previous chapters. It can be seen that the light soaking effect remains stable under the lamination conditions. The η only slightly changes after the pseudo lamination indicating that the thermal budget is too low to result in changes on the solar cell. Compared to the dark annealing at 210 °C discussed in chapter 5.6 the thermal budget of the lamination process is too low to harm the improved solar cells.

To further investigate the impact of the light soaking on the resulting module perfor-

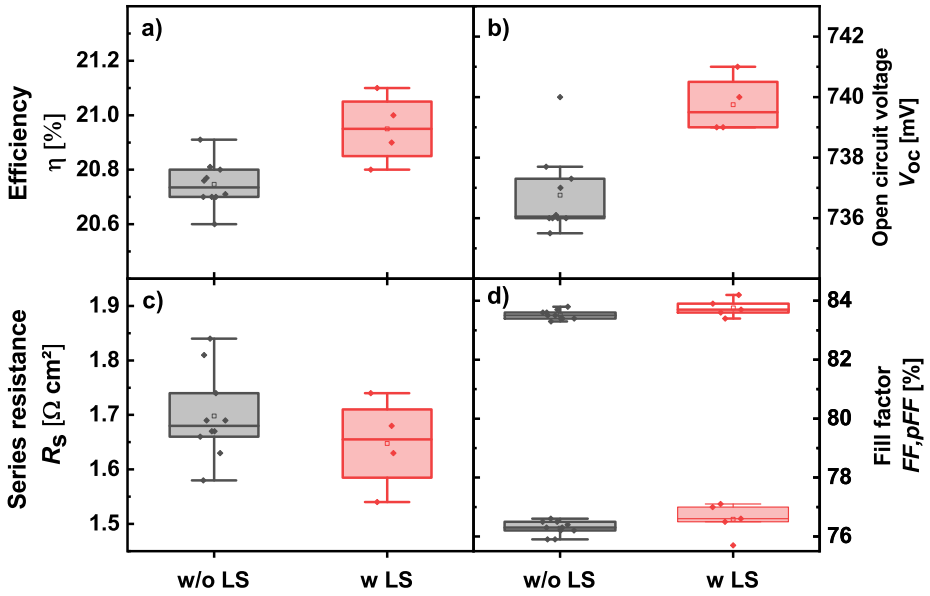

Figure 6.2: Module $J(V)$ parameters of encapsulated solar cells with light soaking and without light soaking for the η,V_{OC}, FF and R_S.

mance, two groups of solar cells with identical initial efficiency and similar V_{OC}×FF are built. The first group undergoes a light soaking treatment (w LS) and the second is directly laminated (w/o LS), and their efficiencies are compared as shown in figure 6.2. The group which underwent the light soaking treatment shows a higher efficiency, as shown in figure 6.2 a). This higher efficiency is mainly obtained by a higher V_{OC}. Besides, the light soaked group shows an increased pFF and decreased R_S and as well obtains a slightly higher FF. The high R_S comes from the additional contacting. The efficiency improvement of the solar cells by light soaking is directly

transferred to the modules' efficiency. All solar cells were laminated in the same process to keep the solar cell to module losses as constant through the batch as possible. It can be concluded that the treated solar cells maintain their gain, which makes the light soaking process feasible for industrial purposes.

6.2 Light soaking treatments on modules

The application of a light soaking treatment on modules is difficult since the used encapsulation materials have a melting point close to 125 °C. Therefore, the light soaking process has to be adapted to a lower temperature and therefore lower intensities to not exceed the temperature limits. A melting of the TPO could be potentially harmful for the encapsulation and have negative impacts on the module's power conversion efficiency. The temperature on the module's surface was measured in dependence of the illumination intensity. A temperature of ~ 100 °C on the module surface is obtained after a 90 s treatment at 30 kW/m^2 while keeping the heating table temperature as low as possible. Therefore, the intensity will be limited to an input intensity of 20 kW/m^2 resulting in a module surface temperature of 50 °C. For this as a starting point, a treatment duration of 90 s was chosen. Two groups of modules are light soaked at low light intensities. The first groups consist of modules with solar cells already light soaking and the second group consists of laminated solar cells without a light soaking treatment. The obtained $J(V)$ results are shown in figure 6.3 a) to d). Over the total accumulated treatment time of 840 s the η, J_{SC} and FF of the modules changes only slightly. For the group without a light soaking, the η reaches a maximum of η = 20.9 %after 360 s which is due to a change in V_{OC}. Due to the temperature limitations, not the same change can be induced on modules as on solar cells. Therefore, the light soaking should be executed on the solar cell.

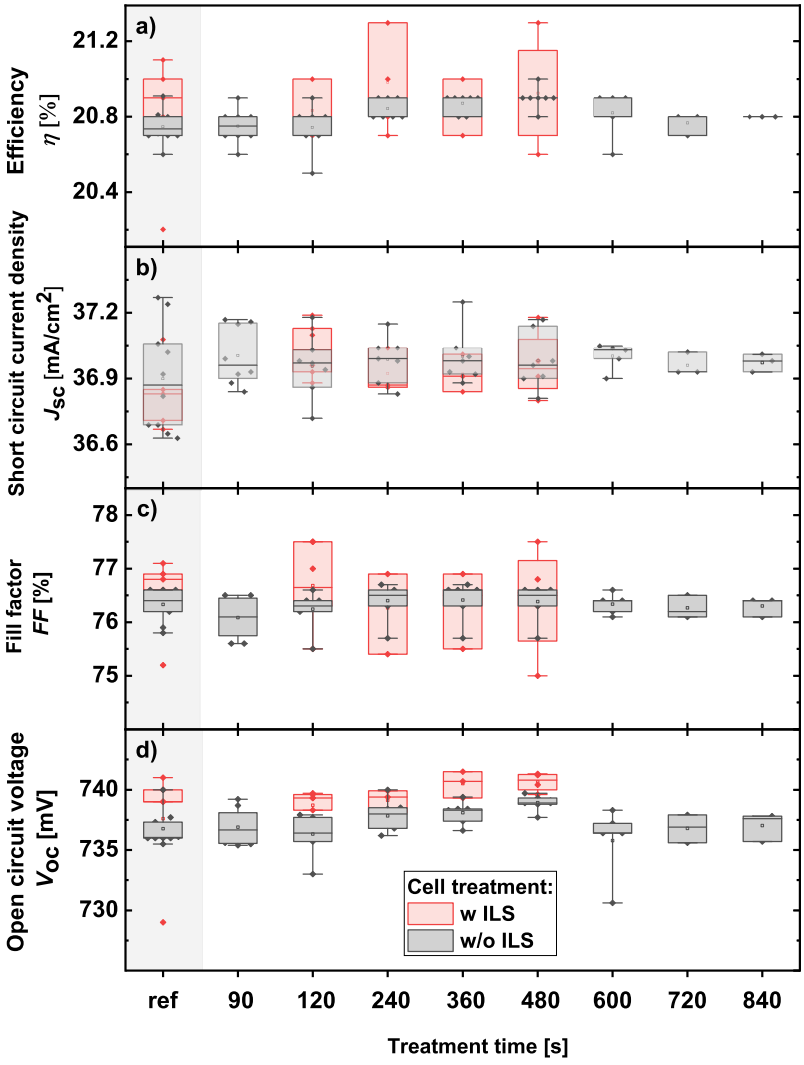

Figure 6.3: Successive low intensity light soaking treatments are applied on modules with solar cells (w/o ILS) and light soaked solar cells (w LS) and their $J(V)$-parameters. In η, J_{SC}, FF and V_{OC} are shown in a) to d) are obtained.

7 Conclusion and Outlook

In this thesis, a thermal-assisted-light-soaking-induced performance increase on SHJ solar cells up to $0.7\%_{\text{abs}}$ could successfully be accomplished. This efficiency increase, under high intensity illumination and 90 s short time, is much larger than that observed previously under 1-sun illumination [19]. The observed efficiency increase often comes from V_{OC} and FF, which are related to the passivation and carrier transport improvement. The light soaking process is broken down into thermal and light effects. While the thermal effect is mainly observed through a decrease of the R_{S} which partially impacts the FF, the light soaking induces a passivation improvement which impacts the V_{OC} and the pFF and therefore the FF. A wide range of material properties could be investigated in terms of electric and passivation properties. It could be revealed that the light soaking effect is not related to the incident photons onto a thin film layer, more to the presence of injected charge carriers. It was observed that the efficiency gain is not only dependent on the light soaking parameters as intensity and temperature itself it is even more dependent on the SHJ solar cell preparation. The underlying mechanisms of the thermal effect on decreasing the R_{S}, which is explained by lowered contact resistance on both contacts, is discussed. The conductivity of (n)a-Si:H degrades due to light-induced defects, meanwhile can be cured by the thermal annealing during the process. For (p)a-Si:H, the increase in boron doping efficiency by light absorption competes with the of thermal treatment. Finally, the carrier transport is mainly dominated by the thermal effect generated during the light soaking process. On the other hand, the performance gain with an increase in a-Si:H/c-Si interface passivation is associated with the injected charge carriers generated from light absorption in wafer bulk. It is shown that the light soaking remains constant over a period of 217 days and is not reset by a lamination process for module fabrication. This work provides a comprehensive understanding of thermal assisted light soaking on SHJ solar cells and gives implications for both academic research and industrial applications. It remains unclear why only a slight change in the ECV of the (n)a-Si:H was observed. The influence of the light soaking on the ITO was attributed to a thermal effect. The observed change in sheet resistance could be further investigated as well as the optical properties. The influence of the hydrogen diffusion into the TCO leave open questions and the hydrogen diffusion properties of ITO are not well known. In cycling a variation of R_{S} could be barely seen, this variation should be further investigated. The role of hydrogen stays unclear since in the SIMS and effusion measurements no changes in the hydrogen content are visible. One solution is to prepare samples with deuterium implanted and investigate in the deuterium diffusion.

A Appendix

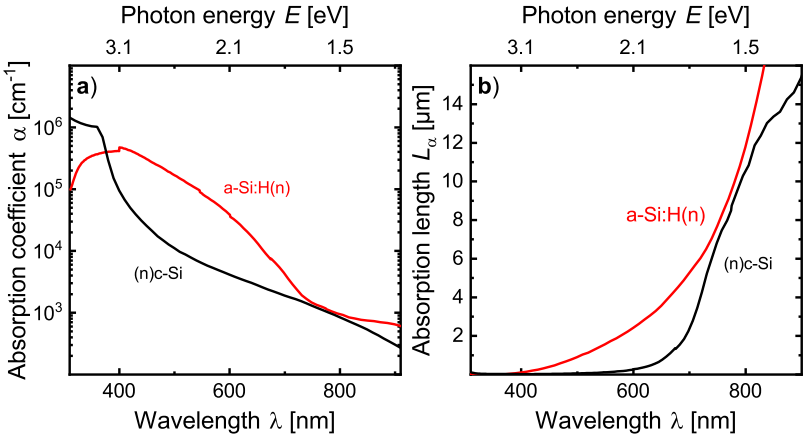

Figure A.1: In a) the absorption coefficient and in b) the absorption length of c-Si and (n)a-Si:H is shown.

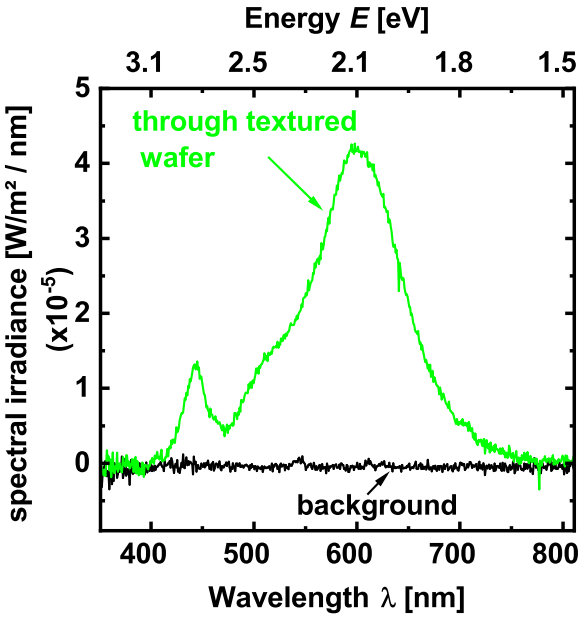

Figure A.2: Spectral irradiance of the LiSO measured with an Ulbricht sphere covered with a textured wafer.

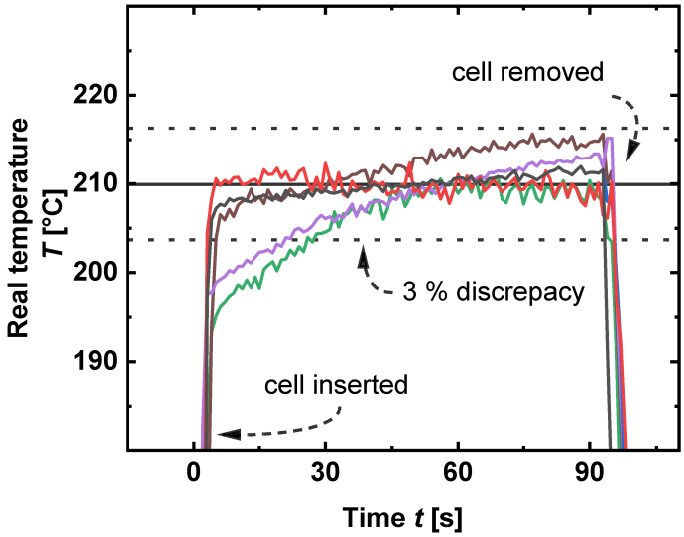

Figure A.3: Temperature measurement of a light soaking process using a thermocouple applied on the solar cell. In some measurements, an increase of the temperature over the first 45 s of the process is observed.

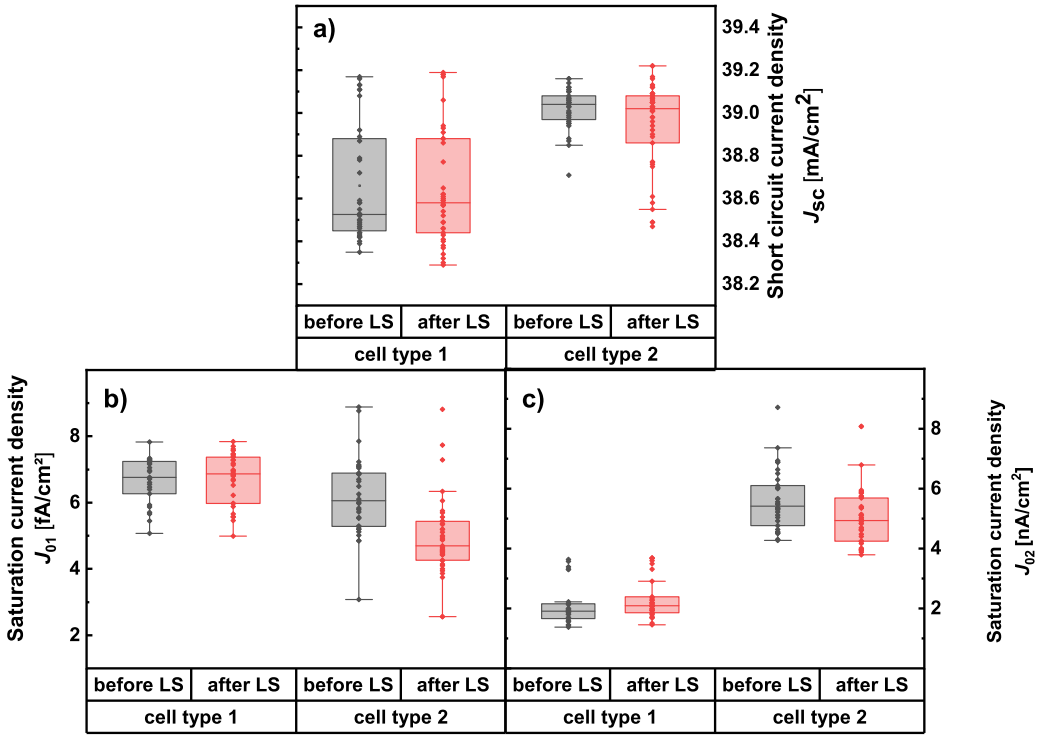

Figure A.4: a) J_{SC}, b) J_{01} and c) J_{02} parameters of light soaked solar cells with different preparations. The "cell type 1" underwent a hydrogen plasma pretreatment before (i)a-Si:H deposition in "cell type 2" this was omitted.

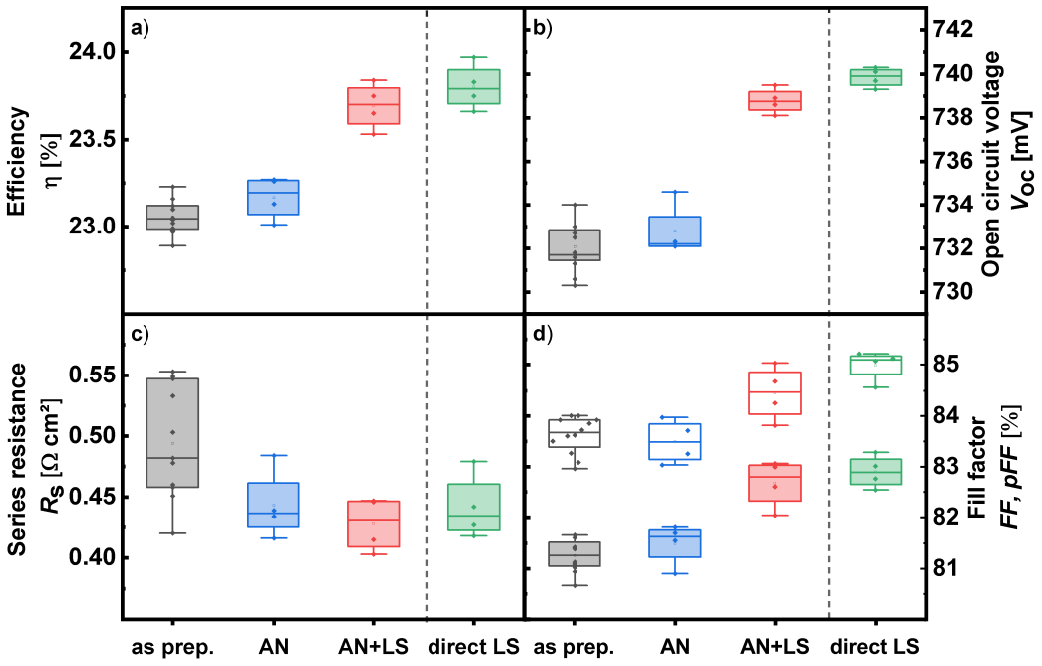

Figure A.5: The results for solar cells either annealed (blue, AN) and then light soaked (red, AN+LS) or directly light soaked (direct LS) are shown. The η, V_{OC}, R_S, FF (filled boxes) and pFF (empty boxes) are shown in a) to d).

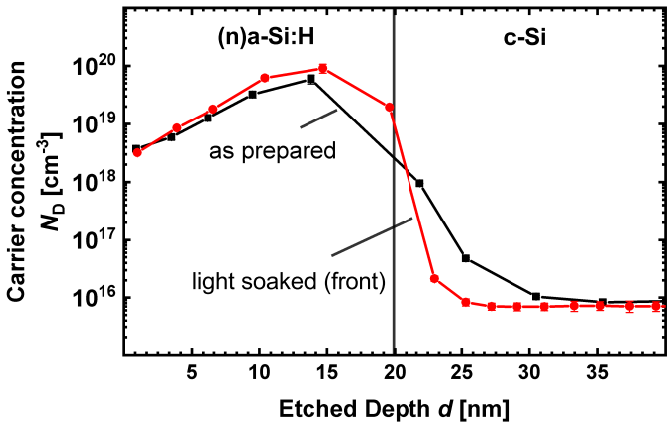

Figure A.6: ECV measurements of thin n-layers before and after light soaking illuminated from the layer side on polished FZ wafers. The carrier concentration N_D of the a (n)a-Si:H layer versus the etching depth d.

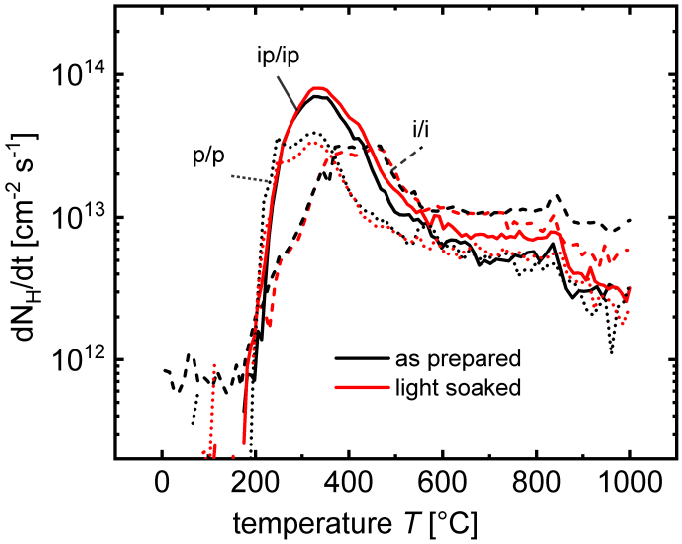

Figure A.7: Hydrogen effusion rate dN_H/dt as a function of temperature T for several symmetrical intrinsic and p-doped a-Si:H layers (i/i, p/p and ip/ip) films, measured with a heating rate of 20 °C/min.

Bibliography

[1] P. Shukla, S. J., R. Slade, A. A. Khourdajie, v. D. R., D. McCollum, M. Pathak, S. Some, P. Vyas, R. Fradera, M. Belkacemi, A. Hasija, G. Lisboa, S. Luz, and J. Malley, *IPCC, 2022: Climate Change 2022: Mitigation of Climate Change. Contribution of Working Group III to the Sixth Assessment Report of the Intergovernmental Panel on Climate Change*, Cambridge University Press, Cambridge, UK and New York, NY, USA (2022).

[2] *The Paris Agreement*, UNFCCC (2015).

[3] *Photovoltaics Report*, Fraunhofer Institute for Solar Energy Systems ISE and PSE Conferences and Consulting GmbH (2020).

[4] *Snapshot of Global PV Markets 2022*, Technical Report (IEA) (2022).

[5] D. B. Needleman, J. R. Poindexter, R. C. Kurchin, I. Marius Peters, G. Wilson, and T. Buonassisi, *Economically sustainable scaling of photovoltaics to meet climate targets*, Energy Environ. Sci. **9** (2016).

[6] M. Taguchi, K. Kawamoto, S. Tsuge, T. Baba, H. Sakata, M. Morizane, K. Uchihashi, N. Nakamura, S. Kiyama, and O. Oota, *HITTM cells high efficiency crystalline Si cells with novel structure*, Progress in Photovoltaics: Research and Applications **8** (2000).

[7] M. A. Green, E. D. Dunlop, J. Hohl-Ebinger, M. Yoshita, N. Kopidakis, and X. Hao, *Solar cell efficiency tables (version 59)*, Progress in Photovoltaics: Research and Applications **30** (2022).

[8] *"LONGi breaks world record for HJT solar cell efficiency twice in one week"*, URL: `https://en.longi-solar.com/home/events/press_detail/id/364.html`, (accessed: 06.02.2022).

[9] K. Yoshikawa, W. Yoshida, T. Irie, H. Kawasaki, K. Konishi, H. Ishibashi, T. Asatani, D. Adachi, M. Kanematsu, H. Uzu, and K. Yamamoto, *Exceeding conversion efficiency of 26% by heterojunction interdigitated back contact solar cell with thin film Si technology*, Solar Energy Materials and Solar Cells **173** (2017).

[10] K. Yoshikawa, H. Kawasaki, Y. Wataru, I. Toru, K. Katsunori, N. Kunihiro, U. Toshihiko, A. Daisuke, K. Masanori, U. Hisashi, and Y. Kenji, *Silicon heterojunction solar cell with interdigitated back contacts for a photoconversion efficiency over 26%*, Nature Energy **2** (2017).

[11] J. Haschke, O. Dupré, M. Boccard, and C. Ballif, *Silicon heterojunction solar cells: Recent technological development and practical aspects - from lab to industry*, Solar Energy Materials and Solar Cells **187** (2018).

[12] Y. Liu, Y. Li, Y. Wu, G. Yang, L. Mazzarella, P. Procel-Moya, A. C. Tamboli, K. Weber, M. Boccard, O. Isabella, X. Yang, and B. Sun, *High-Efficiency Silicon Heterojunction Solar Cells: Materials, Devices and Applications*, Materials Science and Engineering: R: Reports **142** (2020).

[13] A. Razzaq, T. G. Allen, W. Liu, Z. Liu, and S. D. Wolf, *Silicon heterojunction solar cells: Techno-economic assessment and opportunities*, Joule **6** (2022).

[14] S. D. Wolf, A. Descoeudres, Z. C. Holman, and C. Ballif, *High-efficiency Silicon Heterojunction Solar Cells: A Review*, Green **2** (2012).

[15] D. L. Staebler and C. R. Wronski, *Reversible conductivity changes in discharge-produced amorphous Si*, Applied Physics Letters **31** (1977).

[16] S. De Wolf, B. Demaurex, A. Descoeudres, and C. Ballif, *Very fast light-induced degradation of a-Si:H/c-Si(100) interfaces*, Phys. Rev. B **83** (2011).

[17] S. De Wolf, C. Ballif, and M. Kondo, *Kinetics of a-Si:H bulk defect and a-Si:H/c-Si interface-state reduction*, Phys. Rev. B **85** (2012).

[18] E. Kobayashi, S. De Wolf, J. Levrat, G. Christmann, A. Descoeudres, S. Nicolay, M. Despeisse, Y. Watabe, and C. Ballif, *Light-induced performance increase of silicon heterojunction solar cells*, Applied Physics Letters **109** (2016).

[19] E. Kobayashi, S. De Wolf, J. Levrat, A. Descoeudres, M. Despeisse, F.-J. Haug, and C. Ballif, *Increasing the efficiency of silicon heterojunction solar cells and modules by light soaking*, Solar Energy Materials and Solar Cells **173** (2017).

[20] S. Bao, L. Yang, J. Huang, Y. Bai, J. Yang, J. Wang, L. Lu, L. Feng, X. Bai, F. Ren, D. Li, and H. Jia, *The rapidly reversible processes of activation and deactivation in amorphous silicon heterojunction solar cell under extensive light soaking*, Journal of Materials Science: Materials in Electronics **32** (2021).

[21] P. Mahtani, R. Varache, B. Jovet, C. Longeaud, J.-P. Kleider, and N. P. Kherani, *Light induced changes in the amorphous-crystalline silicon heterointerface*, Journal of Applied Physics **114** (2013).

[22] J. Cattin, L.-L. Senaud, J. Haschke, B. Paviet-Salomon, M. Despeisse, C. Ballif, and M. Boccard, *Influence of Light Soaking on Silicon Heterojunction Solar Cells With Various Architectures*, IEEE Journal of Photovoltaics **11** (2021).

[23] S. Olibet, E. Vallat-Sauvain, and C. Ballif, *Model for a-Si:H/c-Si interface recombination based on the amphoteric nature of silicon dangling bonds*, Phys. Rev. B **76** (2007).

[24] M. Wright, A. Soeriyadi, B. Wright, D. Andronikov, I. Nyapshaev, S. Abolmasov, A. Abramov, and B. Hallam, *High-Intensity Illuminated Annealing of Industrial SHJ Solar Cells: A Pilot Study*, IEEE Journal of Photovoltaics **12** (2022).

[25] D. Chen, W. Weigand, M. Wright, M. Kim, J. Shi, Z. J. Yu, B. V. Stefani, A. Soeriyadi, Z. Holman, and B. Hallam, *Evaluating the Impact of and Solutions to Light-induced Degradation in Silicon Heterojunction Solar Cells*, 2019 IEEE 46th Photovoltaic Specialists Conference (PVSC) (2019).

[26] C. Madumelu, B. Wright, A. Soeriyadi, M. Wright, D. Chen, B. Hoex, and B. Hallam, *Investigation of light-induced degradation in N-Type silicon heterojunction solar cells during illuminated annealing at elevated temperatures*, Solar Energy Materials and Solar Cells **218** (2020).

[27] M. Stutzmann, W. B. Jackson, and C. C. Tsai, *Light-induced metastable defects in hydrogenated amorphous silicon: A systematic study*, Phys. Rev. B **32** (1985).

[28] J. Jang, S. C. Park, S. C. Kim, and C. Lee, *Increase of doping efficiency by light soaking in boron-doped hydrogenated amorphous silicon*, Applied Physics Letters **51** (1987).

[29] W. Liu, J. Shi, L. Zhang, A. Han, S. Huang, X. Li, J. Peng, Y. Yang, Y. Gao, J. Yu, K. Jiang, X. Yang, Z. Li, W. Zhao, J. Du, X. Song, J. Yin, J. Wang, Y. Yu, and Z. Liu, *Light-induced Activation of Boron Doping in Hydrogenated Amorphous Silicon for Over 25% Efficiency Silicon Solar Cells*, Nature Energy **7** (2022).

[30] E. Yablonovitch, T. Gmitter, R. M. Swanson, and Y. H. Kwark, *A 720 mV open circuit voltage SiOx:c-Si:SiOx double heterostructure solar cell*, Applied Physics Letters **47** (1985).

[31] A. Richter, M. Hermle, and S. W. Glunz, *Reassessment of the Limiting Efficiency for Crystalline Silicon Solar Cells*, IEEE Journal of Photovoltaics **3** (2013).

[32] M. Taguchi, A. Yano, S. Tohoda, K. Matsuyama, Y. Nakamura, T. Nishiwaki, K. Fujita, and E. Maruyama, *24.7% Record Efficiency HIT Solar Cell on Thin Silicon Wafer*, IEEE Journal of Photovoltaics **4** (2014).

[33] P. Würfel, *Physics of Solar Cells: From Principles to New Concepts*, WILEY-VCH Verlag GmbH & Co. KGaA, 2005, ISBN: 9783527404285.

[34] Z. C. Holman, A. Descoeudres, L. Barraud, F. Z. Fernandez, J. P. Seif, S. D. Wolf, and C. Ballif, *Current Losses at the Front of Silicon Heterojunction Solar Cells*, IEEE Journal of Photovoltaics **2** (2012).

[35] H. Fujiwara and M. Kondo, *Effects of a-Si:H layer thicknesses on the performance of a-Si:H/c-Si heterojunction solar cells*, Journal of Applied Physics **101** (2007).

[36] W. Duan, A. Lambertz, K. Bittkau, D. Qiu, K. Qiu, U. Rau, and K. Ding, *A route towards high-efficiency silicon heterojunction solar cells*, Progress in Photovoltaics: Research and Applications **30** (2022).

[37] A. Kanevce and W. K. Metzger, *The role of amorphous silicon and tunneling in heterojunction with intrinsic thin layer (HIT) solar cells*, Journal of Applied Physics **105** (2009).

[38] A. Louwen, W. van Sark, R. Schropp, and A. Faaij, *A Cost Roadmap For Silicon Heterojunction Solar Cells*, Solar Energy Materials and Solar Cells **147** (2016).

[39] A. D. Rose, T. Geipel, D. Eberlein, A. Kraft, and M. Nowottnick, *Interconnection Of Silicon Heterojunction Solar Cells By Infrared Soldering – Solder Joint Analysis And Temperature Study*, (2019).

[40] M. Wolf and H. Rauschenbach, *Series resistance effects on solar cell measurements*, Advanced Energy Conversion **3** (1963).

[41] M. A. Green, *Solar cells—Operating principles, technology and system applications*, Prentice-Hall, 1982, ISBN: 978-0138222703.

[42] E. Centurioni and D. Iencinella, *Role of front contact work function on amorphous silicon/crystalline silicon heterojunction solar cell performance*, IEEE Electron Device Letters **24** (2003).

[43] K.-U. Ritzau, M. Bivour, S. Schröer, H. Steinkemper, P. Reinecke, F. Wagner, and M. Hermle, *TCO work function related transport losses at the a-Si:H/TCO-contact in SHJ solar cells*, Solar Energy Materials and Solar Cells **131** (2014).

[44] S. M. de Nicolás, D. Muñoz, A. Ozanne, N. Nguyen, and P. Ribeyron, *Optimisation of doped amorphous silicon layers applied to heterojunction solar cells*, Energy Procedia **8** (2011).

[45] M. Ghannam, Y. Abdulraheem, and G. Shehada, *Interpretation of the degradation of silicon HIT solar cells due to inadequate front contact TCO work function*, Solar Energy Materials and Solar Cells **145** (2016).

[46] L. Barraud, Z. C. Holman, N. Badel, P. Reiß, A. Descoeudres, C. Battaglia, S. D. Wolf, and C. Ballif, *Hydrogen-doped indium oxide/indium tin oxide bilayers for high-efficiency silicon heterojunction solar cells*, Solar Energy Materials and Solar Cells **115** (2013).

[47] M. Bivour, S. Schröer, and M. Hermle, *Numerical Analysis of Electrical TCO/a-Si:H(p) Contact Properties for Silicon Heterojunction Solar Cells*, Energy Procedia **38** (2013).

[48] T. F. Schulze, L. Korte, E. Conrad, M. Schmidt, and B. Rech, *Electrical transport mechanisms in a-Si:H/c-Si heterojunction solar cells*, Journal of Applied Physics **107** (2010).

[49] M. Ghannam and Y. Abdulraheem, *Electro-Physical Interpretation of the Degradation of the Fill Factor of Silicon Heterojunction Solar Cells Due to Incomplete Hole Collection at the a-Si:H/c-Si Thermionic Emission Barrier*, Applied Sciences **8** (2018).

[50] D. Lachenal, D. Baetzner, W. Frammelsberger, B. Legradic, J. Meixenberger, P. Papet, B. Strahm, and G. Wahli, *Heterojunction and Passivated Contacts: A simple method to extract both n-TCO and p-TCO contacts resistivity*, Energy Procedia **92** (2016).

[51] M. Bivour, *Silicon Heterojunction Solar Cells: Analysis and Basic Understanding*, PhD thesis, 2015.

[52] B. Demaurex, S. De Wolf, A. Descoeudres, Z. Charles Holman, and C. Ballif, *Damage at hydrogenated amorphous/crystalline silicon interfaces by indium tin oxide overlayer sputtering*, Applied Physics Letters **101** (2012).

[53] A. Khanna, T. Mueller, R. A. Stangl, B. Hoex, P. K. Basu, and A. G. Aberle, *A Fill Factor Loss Analysis Method for Silicon Wafer Solar Cells*, IEEE Journal of Photovoltaics **3** (2013).

[54] K. C. Fong, K. R. McIntosh, and A. W. Blakers, *Accurate series resistance measurement of solar cells*, Progress in Photovoltaics: Research and Applications **21** (2013).

[55] J. Schmidt, *Measurement of differential and actual recombination parameters on crystalline silicon wafers*, IEEE Transactions on Electron Devices **46** (1999).

[56] J. Yu, P. S. Leonard, D. Qiu, Y. Zhao, A. Lambertz, C. Zahren, L. Volker, W. Duan, J. Yu, and K. Ding, *Light-induced performance of SHJ solar modules under 2000 h illumination*, Solar Energy Materials and Solar Cells **235** (2022).

[57] R. A. Sinton and A. Cuevas, *Contactless determination of current–voltage characteristics and minority-carrier lifetimes in semiconductors from quasi-steady-state photoconductance data*, Applied Physics Letters **69** (1996).

[58] C. Leendertz, N. Mingirulli, T. F. Schulze, J. P. Kleider, B. Rech, and L. Korte, *Discerning Passivation Mechanisms at a-si:h/c-si Interfaces by Means of Photoconductance Measurements*, Applied Physics Letters **98** (2011).

[59] D. K. Schroder, *Semiconductor Material and Device Characterization, Third Edition*, John Wiley & Sons, Inc., 2005, ISBN: 9780471739067.

[60] F. M. Smits, *Measurement of sheet resistivities with the four-point probe*, The Bell System Technical Journal **37** (1958).

[61] B. Hallam and C. Chan, *Hydrogen Passivation and Laser Doping for Silicon Solar Cells*, Energy Engineering, Institution of Engineering and Technology, 2021, ISBN: 978-1785616235.

[62] H. Fujiwara, *Spectroscopic ellipsometry: principles and applications*, John Wiley & Sons, 2007, ISBN: 978-0-470-01608-4.

[63] W. Beyer, J. Herion, and H. Wagner, *Fermi energy dependence of surface desorption and diffusion of hydrogen in a-Si: H*, Journal of Non-Crystalline Solids **114** (1989).

[64] W. Beyer, *Hydrogen effusion: a probe for surface desorption and diffusion*, Physica B: Condensed Matter **170** (1991).

[65] B. Hallam, D. Chen, J. Shi, R. Einhaus, Z. C. Holman, and S. Wenham, *Pre-Fabrication Gettering and Hydrogenation Treatments for Silicon Heterojunction Solar Cells: A Possible Path to >700 mV Open-Circuit Voltages Using Low-Lifetime Commercial-Grade p-Type Czochralski Silicon*, Solar RRL **2** (2018).

[66] E. M. El Mhamdi, J. Holovsky, B. Demaurex, C. Ballif, and S. De Wolf, *Is light-induced degradation of a-Si:H/c-Si interfaces reversible?*, Applied Physics Letters **104** (2014).

[67] S. Bernardini and M. I. Bertoni, *Insights into the Degradation of Amorphous Silicon Passivation Layer for Heterojunction Solar Cells*, Physica Status Solidi (a) **216** (2019).

[68] H. M. Branz, R. Reedy, R. S. Crandall, H. Mahan, Y. Xu, and B. P. Nelson, *Fermi-level dependence of the charge state of diffusing hydrogen in amorphous silicon*, Journal of Non-Crystalline Solids **299-302** (2002).

[69] W. Favre, J. Coignus, N. Nguyen, R. Lachaume, R. Cabal, and D. Muñoz, *Influence of the transparent conductive oxide layer deposition step on electrical properties of silicon heterojunction solar cells*, Applied Physics Letters **102** (2013).

[70] C. Luderer, C. Messmer, M. Hermle, and M. Bivour, *Transport Losses at the TCO/a-Si:H/c-Si Heterojunction: Influence of Different Layers and Annealing*, IEEE Journal of Photovoltaics **10** (2020).

[71] J. Schüttauf, C. van der Werf, I. Kielen, W. van Sark, J. Rath, and R. Schropp, *Improving the performance of amorphous and crystalline silicon heterojunction solar cells by monitoring surface passivation*, Journal of Non-Crystalline Solids **358** (2012).

[72] L. Martini, L. Serenelli, F. Menchini, M. Izzi, and M. Tucci, *Silicon heterojunction solar cells toward higher fill factor*, Progress in Photovoltaics: Research and Applications **28** (2020).

[73] Z. Wu, W. Duan, A. Lambertz, D. Qiu, M. Pomaska, Z. Yao, U. Rau, L. Zhang, Z. Liu, and K. Ding, *Low-resistivity p-type a-Si:H/AZO hole contact in high-efficiency silicon heterojunction solar cells*, Applied Surface Science **542** (2021).

[74] *Präzisions Glas & Optik GmbH*, URL: `https://www.pgo-online.com/de/eagle2000.html`, (accessed: 30.05.2022).

[75] W. Haynes, D. Lide, and T. Bruno, *CRC Handbook of Chemistry and Physics*, vol. 97, CRC Press, 2016, ISBN: 978-1498754286.

[76] J. Haschke, C. Messmer, J. Cattin, M. Bivour, M. Boccard, and C. Ballif, *Injection-dependent lateral resistance in front-junction solar cells with nc-Si:H and a-Si:H hole selective contact*, 2019 IEEE 46th Photovoltaic Specialists Conference (PVSC) (2019).

[77] P. Muralidharan, M. A. Leilaeioun, W. Weigand, Z. C. Holman, S. M. Goodnick, and D. Vasileska, *Understanding Transport in Hole Contacts of Silicon Heterojunction Solar Cells by Simulating TLM Structures*, IEEE Journal of Photovoltaics **10** (2020).

[78] S. Huang, W. Liu, X. Li, Z. Li, Z. Wu, W. Huang, Y. Yang, K. Jiang, J. Shi, L. Zhang, F. Meng, and Z. Liu, *Prolonged Annealing Improves Hole Transport of Silicon Heterojunction Solar Cells*, Physica Status Solidi RRL **15** (2021).

[79] O. Madani Ghahfarokhi, K. Chakanga, S. Geissendoerfer, O. Sergeev, K. von Maydell, and C. Agert, *DC-sputtered ZnO:Al as transparent conductive oxide for silicon heterojunction solar cells with μc-Si:H emitter*, Progress in Photovoltaics: Research and Applications **23** (2015).

[80] C. Messmer, M. Bivour, C. Luderer, L. Tutsch, J. Schön, and M. Hermle, *Influence of Interfacial Oxides at TCO/Doped Si Thin Film Contacts on the Charge Carrier Transport of Passivating Contacts*, IEEE Journal of Photovoltaics **10** (2020).

[81] A. Cruz, F. Ruske, A. Eljarrat, P. P. Michalowski, A. B. Morales-Vilches, S. Neubert, E.-C. Wang, C. T. Koch, B. Szyszka, R. Schlatmann, and B. Stannowski, *Influence of Silicon Layers on the Growth of ITO and AZO in Silicon Heterojunction Solar Cells*, IEEE Journal of Photovoltaics **10** (2020).

[82] J. Veirmann, A. Kinfack Leoga, L. Basset, F. W., B. O., and L. P. A., *Understanding The Improvement Of Silicon Heterojunction Solar Cell Under Light Soaking*, SiliconPV Conference (2021).

[83] N. Hata and S. Wagner, *A comprehensive defect model for amorphous silicon*, Journal of Applied Physics **72** (1992).

[84] N. Hata, P. Stradins, C. Fortmann, H. Fujiwara, M. Fujiwara, and A. Matsuda, *Light-induced, reversible, above-gap, optical changes in hydrogenated amorphous silicon films*, Journal of Non-Crystalline Solids **266-269** (2000).

Zentrales Prüfungsamt/Central Examination Office

Eidesstattliche Versicherung
Statutory Declaration in Lieu of an Oath

Rudolph, Tobias

Name, Vorname/Last Name, First Name

Matrikelnummer (freiwillige Angabe)
Matriculation No. (optional)

Ich versichere hiermit an Eides Statt, dass ich die vorliegende Arbeit/Bachelorarbeit/ Masterarbeit* mit dem Titel
I hereby declare in lieu of an oath that I have completed the present paper/Bachelor thesis/Master thesis* entitled

Application of Intensive Light Soaking on Silicon Heterojunction Solar Cells and Modules

selbstständig und ohne unzulässige fremde Hilfe (insbes. akademisches Ghostwriting) erbracht habe. Ich habe keine anderen als die angegebenen Quellen und Hilfsmittel benutzt. Für den Fall, dass die Arbeit zusätzlich auf einem Datenträger eingereicht wird, erkläre ich, dass die schriftliche und die elektronische Form vollständig übereinstimmen. Die Arbeit hat in gleicher oder ähnlicher Form noch keiner Prüfungsbehörde vorgelegen.
independently and without illegitimate assistance from third parties (such as academic ghostwriters). I have used no other than the specified sources and aids. In case that the thesis is additionally submitted in an electronic format, I declare that the written and electronic versions are fully identical. The thesis has not been submitted to any examination body in this, or similar, form.

Aachen, 03.06.2022

Ort, Datum/City, Date

T. Rudolph

Unterschrift/Signature

*Nichtzutreffendes bitte streichen

*Please delete as appropriate

Belehrung:
Official Notification:

§ 156 StGB: Falsche Versicherung an Eides Statt
Wer vor einer zur Abnahme einer Versicherung an Eides Statt zuständigen Behörde eine solche Versicherung falsch abgibt oder unter Berufung auf eine solche Versicherung falsch aussagt, wird mit Freiheitsstrafe bis zu drei Jahren oder mit Geldstrafe bestraft.
Para. 156 StGB (German Criminal Code): False Statutory Declarations
Whoever before a public authority competent to administer statutory declarations falsely makes such a declaration or falsely testifies while referring to such a declaration shall be liable to imprisonment not exceeding three years or a fine.
§ 161 StGB: Fahrlässiger Falscheid; fahrlässige falsche Versicherung an Eides Statt
(1) Wenn eine der in den §§ 154 bis 156 bezeichneten Handlungen aus Fahrlässigkeit begangen worden ist, so tritt Freiheitsstrafe bis zu einem Jahr oder Geldstrafe ein.
(2) Straflosigkeit tritt ein, wenn der Täter die falsche Angabe rechtzeitig berichtigt. Die Vorschriften des § 158 Abs. 2 und 3 gelten entsprechend.
Para. 161 StGB (German Criminal Code): False Statutory Declarations Due to Negligence
(1) If a person commits one of the offences listed in sections 154 through 156 negligently the penalty shall be imprisonment not exceeding one year or a fine.
(2) The offender shall be exempt from liability if he or she corrects their false testimony in time. The provisions of section 158 (2) and (3) shall apply accordingly.

Die vorstehende Belehrung habe ich zur Kenntnis genommen:
I have read and understood the above official notification:

Aachen, 03.06.2022

Ort, Datum/City, Date

T. Rudolph

Unterschrift/Signature